MOLECULAR BIOLOGY

DNA polymerase δ subunit Pol32 binds histone H3-H4 and couples nucleosome assembly with Okazaki fragment processing

Guojun Shi[1]†, Chaoqi Yang[1,2]†, Jiale Wu[1]†, Yang Lei[1,2], Jiazhi Hu[3], Jianxun Feng[1]*, Qing Li[1]*

During lagging strand chromatin replication, multiple Okazaki fragments (OFs) require processing and nucleosome assembly, but the mechanisms linking these processes remain unclear. Here, using transmission electron microscopy and rapid degradation of DNA ligase Cdc9, we observed flap structures accumulated on lagging strands, controlled by both Pol δ's strand displacement activity and Fen1's nuclease digestion. The distance between neighboring flap structures exhibits a regular pattern, indicative of matured OF length. While *fen1*Δ or enhanced strand displacement activities by polymerase δ (Pol δ; *pol3*$^{exo-}$) minimally affect inter-flap distance, mutants affecting replication-coupled nucleosome assembly, such as *cac1*Δ and *mcm2-3A*, do significantly alter it. Deletion of Pol32, a subunit of DNA Pol δ, significantly increases this distance. Mechanistically, Pol32 binds to histone H3-H4 and is critical for nucleosome assembly on the lagging strand. Together, we propose that Pol32 establishes a connection between nucleosome assembly and the processing of OFs on lagging strands.

INTRODUCTION

In eukaryotes, DNA replication occurs in the context of a chromatin environment. DNA replication is essential for the inheritance of both genetic and epigenetic information (*1*). During DNA replication, the leading-strand DNA is copied continuously, while the lagging strand DNA is synthesized in discrete fragments called Okazaki fragments (OFs) (*2*, *3*). The synthesis of OFs is fast and efficient. It is estimated to take place ~100,000 times during each cell division in yeast (*4*). Therefore, accurately processing OFs is vital for DNA replication and genome integrity (*4*).

A coordinated series of events occur each time an OF is synthesized (*3*). The initiation of OF replication is via an 8- to 12- nucleotide (nt) RNA primer synthesized by the DNA polymerase α-primase complex, which is then extended by the addition of a ~20-nt DNA primer (*3*–*5*). The high-fidelity DNA polymerase δ (Pol δ) subsequently displaces Pol α to synthesize a ~200-nt DNA fragment (*3*, *6*). Pol δ catalyzes the DNA synthesis to extend toward the preceding OF and continues DNA synthesis with strand displacement upon reaching the adjacent OF, leading to the generation of flap structures (*7*, *8*). The strand displacement of Pol δ generally replaces at least 30 nt of DNA to remove the RNA-DNA hybrid synthesized by the error-prone Pol α in the genome after replication (*9*). The resulting flap structure must be removed by several nucleases, such as the flap endonuclease Fen1 (*4*, *10*), Dna2 (*10*, *11*), and Exo1 (*8*, *12*). DNA cleavage produces a nick, which can be sealed by DNA ligase I (Cdc9) to finish the OF processing (*3*). While great details have been elucidated during OF processing, it remains largely unclear how this process coordinated with the nucleosome reassembly process in eukaryotes.

Nucleosome assembly must be tightly coupled to DNA replication (*13*, *14*). Behind the replication fork (RF), nucleosome structures should be reassembled immediately on nascent DNA. This process is termed DNA replication-coupled (RC) nucleosome assembly. It has been reported that OFs are heterogeneously sized with a repeat length corresponding to that of nucleosomes in *Saccharomyces cerevisiae* (*15*). In addition, OF processing during DNA replication is strongly affected by nucleosomes (*15*, *16*). Genome-wide nucleosome mapping has shown that the OF termini are enriched around nucleosome dyad positions (*15*). It has been observed that the junctions can be altered by interfering with chromatin assembly or Pol δ processivity (*15*, *16*). Of note, these mappings were conducted under impaired DNA ligase activity conditions. It has been observed that the positioning of OF termini within the nucleosome is closely associated with the nick translation by prolonged depletion of DNA ligase I (*17*). Therefore, the interplay among Pol δ's activity, histone deposition, and DNA ligase is critical for nucleosome assembly on lagging strands.

To explore further the relationship between OFs and nucleosomes, we used the transmission electron microscopy (TEM) combined with rapid degradation of DNA ligase Cdc9 to directly observe OFs at the RF in *S. cerevisiae*. Our observations indicate that deficiencies in ligating OFs result in an accumulation of flap structures along the lagging strands of the RFs. The length of these flap structures is governed by both the strand displacement activities of Pol δ and the Fen1 nuclease-like enzyme. In addition, the periodic distribution of distances between adjacent flap structures serves as a reflection of matured OFs. While the inter-flap distance increased slightly in Pol δ mutant cells with enhanced strand displacement activity, the inter-flap distance remains unchanged in the absence of Fen1. The deletion of the Pol32 subunit within the Pol δ complex leads to a marked increase in the inter-flap distance. Mechanistically, the Pol32 subunit directly binds histone H3-H4, facilitating nucleosome assembly at the lagging strand. The deletion of Pol32 results in reduced nucleosome occupancy on the lagging strand. These collective findings strongly suggest that the DNA Pol δ complex plays a direct role in nucleosome assembly on lagging strands by binding

[1]State Key Laboratory of Protein and Plant Gene Research, School of Life Sciences and Peking-Tsinghua Center for Life Sciences, Peking University, Beijing 100871, China. [2]Academy for Advanced Interdisciplinary Studies, Peking University, Beijing 100871, China. [3]The MOE Key Laboratory of Cell Proliferation and Differentiation, School of Life Sciences, Genome Editing Research Center, Center for Life Sciences, Peking University, Beijing 100871, China.
*Corresponding author. Email: li.qing@pku.edu.cn (Q.L.); fengjx@pku.edu.cn (J.F.)
†These authors contributed equally to this work.

histone H3-H4. This observation provides direct mechanistic evidence for the coupling of DNA replication to chromatin assembly on lagging strands.

RESULTS

The inability to ligate OFs leads to an accumulation of flap structures on the lagging strands of the RFs

To detect OFs at the RFs, DNA replication intermediates were purified, followed by a benzalkonium chloride (BAC)–mediated spreading and visualized by a TEM (Fig. 1A). OF maturation requires sealing the nick between the OFs by DNA ligase Cdc9 (*15*, *18*, *19*). To differentiate the lagging strand from the leading strand under an electron microscope, we used an auxin-inducible degron (AID*) system to induce a rapid depletion of the DNA ligase-Cdc9 in budding yeast during the early synthesis (S) phase to prevent the ligation of OFs (*20*). Briefly, yeast cells were arrested in the Growth phase 1 (G_1) phase using α-factor for 2 hours, and indole-3-acetic acid (IAA) was applied for 1 hour to degrade Cdc9 before releasing them into the S phase. Cells were then released into the YPD (yeast extract, peptone, and dextrose) medium containing IAA, allowing them to enter the early S phase at 25°C for 35 min (Fig. 1B). The S-phase cells were prepared to visualize DNA RFs. Cdc9 tagged with an AID*-9myc degron was reduced by 89% of its initial level (Fig. 1C).

Consistent with previous observations, we observed two types of replication intermediates: replication bubbles (Fig. 1, D and E, left panels) and Y-shape structures with one RF (Fig. 1, D and E, right panels). Notably, short-flapped DNA was observed in roughly ~94.1% of daughter strands upon IAA-induced Cdc9 degradation (Fig. 1F). These short DNA flaps are found to be enriched at one daughter strand in both bubble-shape and Y-shape structures upon IAA treatment (Fig. 1E), suggesting that these short flaps are generated in a strand-specific fashion and are induced by the Cdc9 degradation. Furthermore, we observed that the flap structures extend from the branching points to more than 5 kb away, with the highest frequency occurring near the branching points (fig. S1A). These data are reminiscent of the flap structures generated on the lagging strands.

To confirm that these short flaps are enriched at the lagging strand, we analyzed whether they co-localized with single-stranded DNA (ssDNA) at the RFs because ssDNA is preferentially enriched at the lagging strands (*21*). We found that 92.4% of ssDNA-containing daughter strands were also capable of detecting flap structures (fig. S1B), supporting the idea that these flaps are enriched at the lagging strands.

The flap distance shows a periodic distribution similar to the OF length

To characterize the flap structure, we first measured the apparent distance between two adjacent flaps, referred to as the "inter-flap distance." The scale bar is normalized by plasmid pRS313 and M13, and the 200-nm scale bar is equal to 500 base pairs (bp) of DNA length (fig. S1C). We observed that the distance ranged from ~50 bp to 3 kb (fig. S1D). Given that a small amount of Cdc9 still functions within the cells, and considering the difficulty in detecting very short flap structures, coupled with the fact that the size of OFs approximates that of a nucleosome in yeast cells (*15*), we analyzed the distribution of inter-flap distances smaller than 600 bp. Our analysis revealed that inter-flap distance in this group predominantly clustered around 190 and 338 bp (Fig. 1, E and G). These sizes prompted us to consider that they might represent mono- or di-OF sizes, corresponding to the lengths of matured OFs.

To further examine the connection between the inter-flap distance and OF length, we narrowed the analysis to analyze the distribution of inter-flap distances smaller than 300 bp and found that they predominantly cluster around the 150- to 200-bp range (Fig. 1, H and I). These results support the idea that these flaps are accumulating due to un-ligated OFs resulting from Cdc9 degradation and the peaked inter-flap distance, reflecting a matured OF length.

Strand displacement by Pol δ is responsive to the generation of DNA flaps

To further characterize the observed flap structures, we analyzed the flap structures and measured the apparent length of the short flaps, which we term "flap length" (Fig. 2A and fig. S2A). In a wild-type (WT) background, we observed flap lengths ranging from 20 to 165 nt, and the mean flap length was around 69 ± 27 nt (Fig. 2, E and F). Given the inherent connections between the location of OF termini and nucleosome midpoints (*15*), we analyzed the distribution of flap lengths that are less than half of the nucleosome size plus a linker DNA between nucleosomes. We analyzed the distribution of flap lengths ranging from 20 to 90 nt, and the distributions predominantly cluster around 39, 52, and 67 nt, respectively (Fig. 2G), indicating a potential interval of about 13 to 15 nt between flap lengths (Fig. 2K). Short DNA flaps are mostly generated by strand displacement synthesis of Pol δ for the removal of the 5′ end of the previous OF and processed by nucleases including Fen1 (*3*). Thus, this observation indicates that the strand displacement synthesis occurs in ~14-nt increments. Alternatively, nuclease digestion may influence the length of the flap. Given the potential barriers posed by nucleosomes in strand displacement synthesis and the 147 bp of DNA wrapped around the histone octamer in a typical nucleosome structure, which includes 14 distinct interaction sites of DNA with histones (*15*, *22*), these results indicate a potential link between nucleosome structure and strand displacement activities.

Previous studies have analyzed the locations of the 5′ and 3′ termini of OFs at various time points after release into S phase under conditions of Cdc9 depletion (*17*). This analysis showed that the 5′ and 3′ termini are initially more separated at earlier time points following Cdc9 degradation, with a shift of ~50 bp in the 5′ termini of OFs away from the nucleosome dyad position at 30 min. However, as time progressed, the termini were found to be more symmetrically distributed around the nucleosome midpoint (*17*). These findings suggest that flap structures are transient intermediates that appear early in the absence of Cdc9 and can be processed later in cells. To avoid potential biases in our assessment of matured OF length due to the transient accumulation of flap structures, we examined flap structures collected from samples 50 min into the S phase (S50). We found that the average flap length was ~65 ± 32 nt (fig. S2, B to D). The distribution of flap lengths ranged from 20 to 90 nt, clustering around 39, 58, and 78 nt (fig. S2, E and F). We noticed that the major peak predominantly clustered around 52 nt in S35 samples but shifted to 39 nt in S50

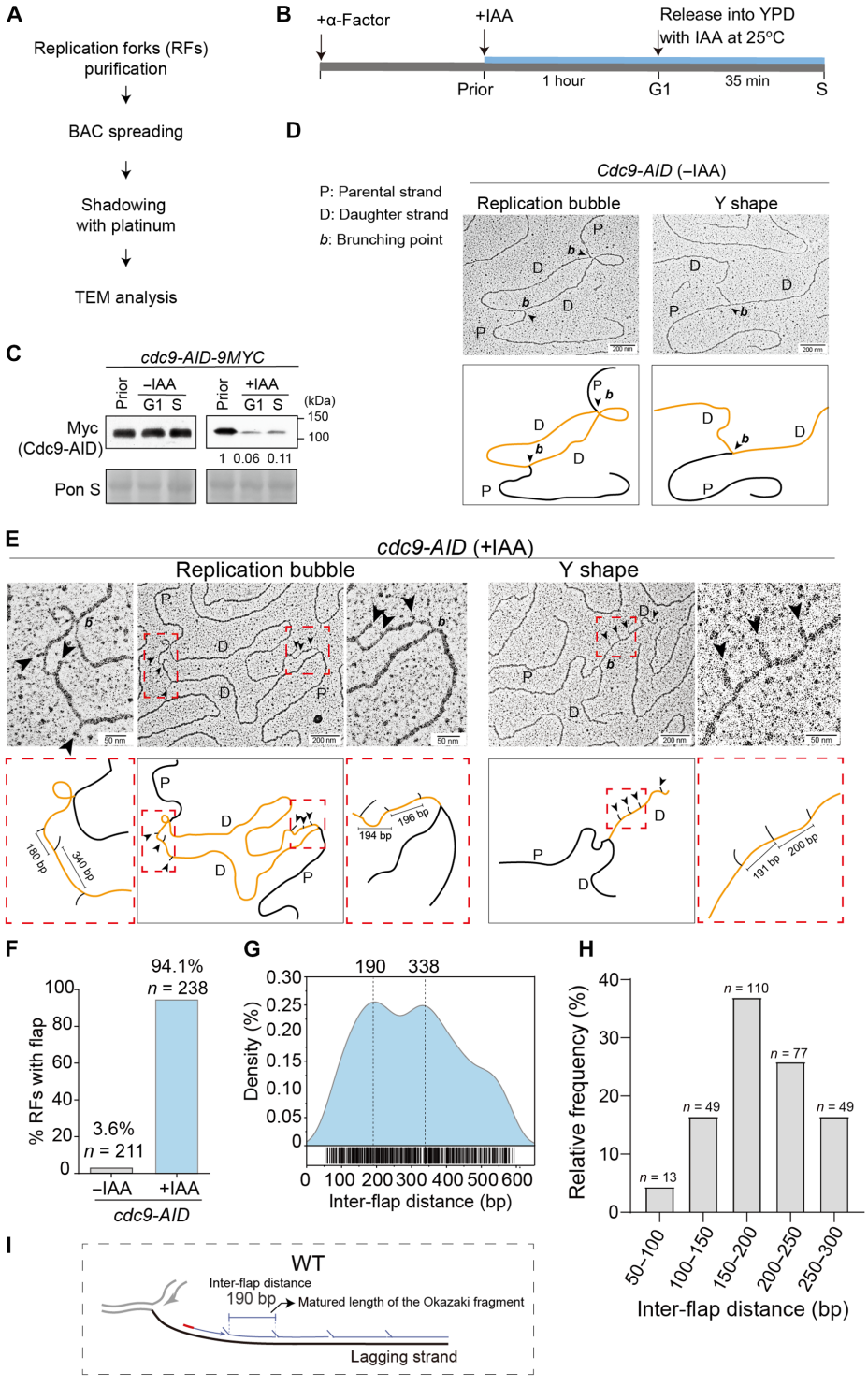

Fig. 1. Cdc9-depletion leads to an accumulation of flap structures on the lagging strands. (**A**) Graphical outline of the transmission electron microscopy (TEM) experimental procedure. (**B**) Outline of the Cdc9-AID* degradation system: Yeast cells arrested in the G_1 phase with α-factor for 2 hours, treated with IAA for 1 hour, and released into the early S phase at 25°C for 35 min. AID*, auxin-inducible degron. (**C**) Cdc9 protein levels analyzed by immunoblotting with antibodies against the AID*-9 × Myc degron. Pon S, Ponceau S staining as a loading control. (**D**) Representative TEM images of normal replication bubble (left) and Y-shape intermediate (right). D, daughter strand; P, parental strand. Scale bars, 200 nm [500 base pairs (bp)]. (**E**) Representative TEM images of a replication bubble (left) and a Y-shaped intermediate (right) in cells after Cdc9 degradation. Diagram of the molecule below the image; enlarged view inside the red dashed square to the side. Black arrowheads point to flap DNA, and flap length is labeled. Scale bars, 200 nm (500 bp) and 50 nm (125 bp). (**F**) Percentage of forks with flaps with (+IAA) or without (–IAA) IAA treatment. $n = 211$ (–IAA) and 238 (+IAA). (**G**) Probability density fitting of flap distances below 600 bp in *cdc9*-AID* cells treated with IAA. (**H**) Distribution of flap distances below 300 bp in 50-bp intervals. (**I**) Cartoon of inter-flap distance and typical matured OF length in wild-type (WT) cells.

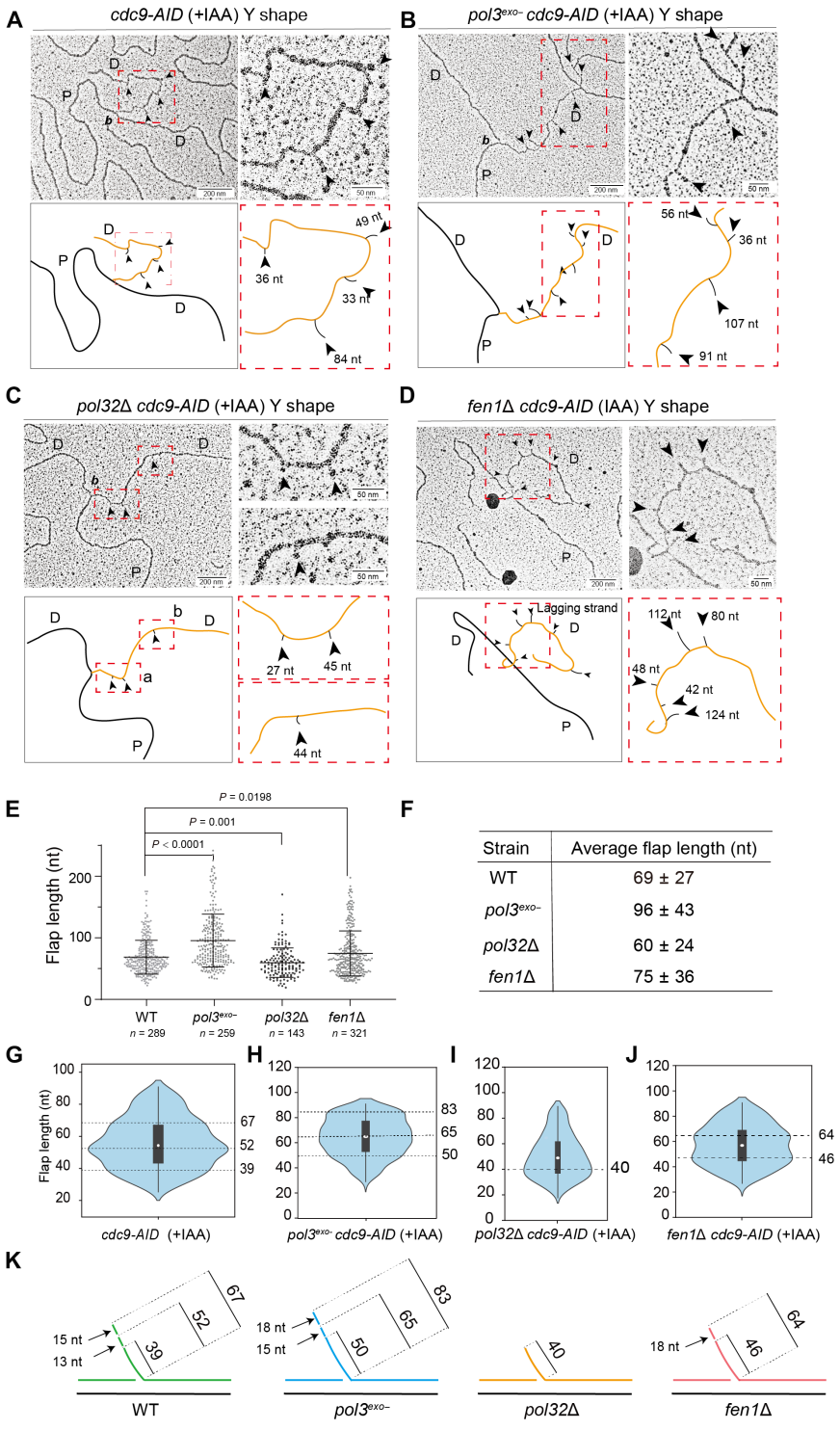

Fig. 2. Pol δ's strand displacement activity and Fen1 affect flap length. (**A** to **D**) Flap length examples in WT, *pol3*$^{exo-}$, *pol32*Δ, and *fen1*Δ replication forks (RFs). Diagram of the molecule below the image; enlarged view inside the red dashed square to the side. Black arrowheads point to flap DNA, and flap length is labeled. Scale bars, 200 nm (500 bp) and 50 nm (125 bp). (**E** and **F**) Average flap length in WT, *pol3*$^{exo-}$, *pol32*Δ, and *fen1*Δ cells from three independent experiments. $n = 289$, 259, 143, and 321, respectively. Bars represent mean with SD. *P* value from an unpaired Student's *t* test. (**G**) Violin plot of flap length distribution in WT cells, with peaks clustered around 39, 52, and 67 nt, respectively. (**H**) Violin plot of flap length distribution in *pol3*$^{exo-}$ cells, with peaks at 50, 65, and 83 nt. (**I**) Violin plot of flap length distribution in *pol32*Δ cells, with a peak at 40 nt. (**J**) Violin plot of flap length distribution in *fen1*Δ cells, with peaks at 46 and 64 nt. (**K**) Cartoon depicting flap length in WT, *pol3*$^{exo-}$, *pol32*Δ, and *fen1*Δ RFs.

samples. This shift supports the idea that flap structures can be processed at later time points.

Further, in S50 samples, flap structures can also be seen more than 5 kb away from the branching points (fig. S3, A and B). We observed a similar trend in the frequency of detecting flaps from the branching point to distant regions, as compared to the S35 samples (fig. S3B). These results indicate that the flap structures are relatively stable within the observed time frame. Analysis of the inter-flap distances ranging from 50 to 600 bp revealed that the first peak they clustered around is 203 bp (fig. S3C). Analysis of the inter-flap distances less than 300 bp showed that they primarily localized within the 150- to 200-bp range (fig. S3D). These results suggest, that although flap structures are transiently generated in the absence of Cdc9 and can be processed later in cells, the observed flap structures are relatively stable within the time frame that we examined. Coupled with statistical analysis based on large samples, this stability enables us to effectively use this system to investigate OF length dynamics. We subsequently chose 35 min after release into the S phase as the primary time point for collecting samples in our subsequent studies.

To test whether the observed short flaps arise from strand displacement activity of Pol δ, we first analyzed the flap structures in *pol3*$^{exo-}$ mutants, which carried a *D520V* mutation at the Pol3 subunit of Pol δ complex (Fig. 2B and fig. S4A). It has been reported that *pol3*$^{exo-}$ mutant is deficient in exonuclease and has excessive strand displacement (*8*, *23*). We found that the average flap length in *pol3*$^{exo-}$ mutant cells was around 96 ± 43 nt (Fig. 2, E and F), which is significantly longer than WT. We measured the flap length and analyzed the distribution of flap lengths ranging from 20 to 90 nt in *pol3*$^{exo-}$ mutants and found that the distributions predominantly cluster around 50, 65, and 83 nt (Fig. 2H). Intriguingly, the clustered length in *pol3*$^{exo-}$ is increased by ~13 nt longer at each peak than the WT (Fig. 2K), supporting the idea that a potential increment of 13- to 15-nt synthesis for strand displacement catalyzed by Pol δ complex.

It was reported that the Pol32 subunit of Pol δ promotes strand displacement activity (*8*). We then visualized the flap structures in *pol32*Δ mutant cells under IAA treatment (Fig. 2C). We measured the flap length and analyzed the distribution of these lengths ranging from 20 to 90 nt and found that the mean flap length in *pol32*Δ mutant cells is around 60 ± 24 nt (Fig. 2, E and F). While the mean value of flap length is apparently shorter than in the WT, the distributions predominantly cluster around 40 nt (Fig. 2, I and K), which is close to the shortest one in the WT S35. These results are consistent with the idea that defects in strand displacement activity result in shorter flap structures.

Flap structures are processed by several nucleases before DNA ligation during OF maturation. Fen1 is one of the major endonucleases that is involved in the flap structure processing during OF maturation (*3*, *4*, *14*). An accumulation of long flap structures at ~1 to 2% of OF termini was previously observed in fission yeast (*14*). We analyzed the flap structures in *fen1*Δ mutant cells under IAA treatment (Fig. 2D and fig. S4B). We found that the mean flap length in *fen1*Δ mutant cells was around 75 ± 36 nt (Fig. 2F) and that the distributions predominantly cluster around 46 and 64 nt, respectively (Fig. 2J), which is mildly longer than WT. This indicates that the flap structures that we observed under Cdc9 degradation have likely been processed by nuclease digestion, which is involved in the function of Fen1 in this process.

Pol32 is required for the control of the matured length of the OF

To interrogate the regulation mechanism underlying the matured length of OFs, we analyzed the inter-flap distance in various mutant backgrounds in the Cdc9-degradation condition. Given that Cdc9 degradation does not result in complete depletion and that a few ligation events can still occur, as well as the difficulty in detecting very short flap structures, these factors might influence the inter-flap distances that we measured. Initially, we compared the inter-flap distances measured in *fen1*Δ mutant cells. We analyzed the distribution of inter-flap distances smaller than 600 bp and found that the inter-flap distance in *fen1*Δ cells centered around 190 bp (Fig. 3, A, B, and J), resembling the first peak of the clustered flap distance in WT cells. Notably, the flap distance in *fen1*Δ cells was quite concentrated closely near the first peak, without the second peak observed. Moreover, we analyzed the distribution of inter-flap distances smaller than 300 bp and found that they predominantly cluster around the 150- to 200-bp range (Fig. 3C). Furthermore, we observed a similar trend in the frequency of detecting flaps from the branching point to distant regions as seen in the WT S35 samples. However, in the distant regions, the frequency is relatively higher than in WT S35 cells (fig. S4, B and C). In addition, the average number of flaps detected within 3 kb from the branching points is increased compared to WT cells (fig. S4D). These results further support the idea that Fen1's activity is required in the flap structure processing, and deletion of Fen1 may enhance the detection of short flap structures that accumulate on the lagging strands.

Next, we observed that the inter-flap distance in *pol3*$^{exo-}$ mutant cells peaked at around 210 bp (Fig. 3, D, E, and J). Analysis of inter-flap distances less than 300 bp revealed that they primarily fell within the 150- to 200-bp range (Fig. 3F), similar to those observed in WT samples. Notably, the inter-flap distance in *pol32*Δ mutant cells was found to cluster around 280 bp (Fig. 3, G, H, and J). Analysis of the inter-flap distances less than 300 bp showed that they primarily localized within the 200- to 300-bp range (Fig. 3I). Consistent with this observation, the average number of detected flaps within 3 kb from the branching point is markedly decreased in *pol32*Δ mutant cells (fig. S4D). Thus, the inter-flap distance in *pol32*Δ mutant cells is apparently longer than it is in WT cells, reflecting that the matured length of the OF is markedly increased in this mutant background.

The observed alterations in the inter-flap distance between the WT and *pol32*Δ mutants were unlikely due to differences in Cdc9 degradation efficiency, as the percentage of replication intermediates with flaps between the WT and the two Pol δ mutant cells were similar (fig. S4, E and F). Collectively, these findings indicate that, while Pol δ is crucial for strand displacement synthesis during OF maturation, its Pol32 subunit regulates the length of the matured OFs.

The matured length of the OF is influenced by both newly synthesized histone deposition and parental histone transferring

To rule out that the potential effect on the very short flap structures can be processed and hard to detect, we attempted to construct the

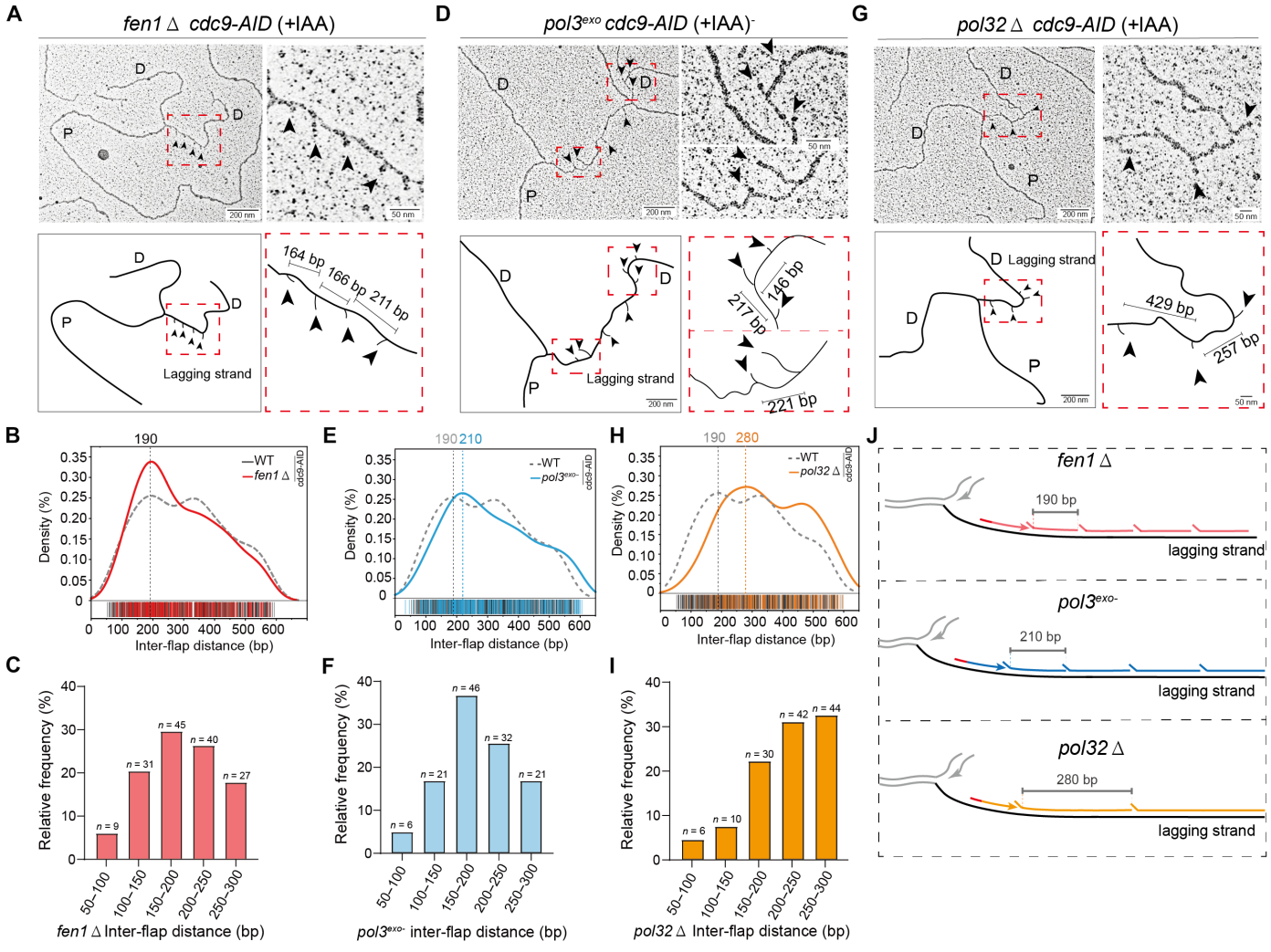

Fig. 3. Pol32 is required to maintain the inter-flap distance. (**A**) Inter-flap distance examples in *fen1*Δ cells' RFs. Diagram of the molecule below the image; enlarged view inside the red dashed square to the side. Black arrowheads point to flap DNA, and flap length is labeled. Scale bars, 200 nm (500 bp) and 50 nm (125 bp). (**B**) Probability density fitting of inter-flap distance in *fen1*Δ cells. (**C**) Percentage of inter-flap distance below 300 bp in 50-bp intervals in *fen1*Δ cells. (**D**) Inter-flap distance examples in *pol3*$^{exo-}$ RFs. Diagram of the molecule below the image; enlarged view inside the red dashed square to the side. Black arrowheads point to flap DNA, and flap length is labeled. Scale bars, 200 nm (500 bp) and 50 nm (125 bp). (**E**) Probability density fitting of the inter-flap distance in *pol3*$^{exo-}$ cells. (**F**) Percentage of inter-flap distance below 300 bp in 50-bp intervals in *pol3*$^{exo-}$ cells. (**G**) Inter-flap distance examples in *pol32*Δ RFs. Diagram of the molecule below the image; enlarged view inside the red dashed square to the side. Black arrowheads point to flap DNA, and flap length is labeled. Scale bars, 200 nm (500 bp) and 50 nm (125 bp). (**H**) Probability density fitting of inter-flap distance in *pol32*Δ cells. (**I**) The percentage of inter-flap distance below 300 bp in 50-bp intervals in *pol32*Δ cells. (**J**) Cartoon depicting inter-flap distance in *fen1*Δ, *pol3*$^{exo-}$, and *pol32*Δ RFs.

*pol32*Δ *fen1*Δ cells and found that the *pol32*Δ *fen1*Δ double mutant is lethal (fig. S5), indicating that Fen1's activity is required in the absence of Pol32. If this were the sole explanation for the increased inter-flap distance in the *pol32*Δ background, then we would expect to observe a clustered peak resembling a WT pattern but in a di-OF size when analyzing the distribution of inter-flap distances, given the large numbers that we measured. However, the 280-bp peak is clearly bigger than the mono-OF size and shorter than the typical di-OF size. On the basis of the clustered peak patterns that we observed in *pol32*Δ cells, considering that it was established that the nucleosome assembly level affects the OF length (*15*), we, therefore, hypothesize that Pol32 has a role in nucleosome assembly.

To test this idea, we first observed the flap structures in two nucleosome assembly–defective mutant cells, *cac1*Δ and *mcm2-3A*. CAF-1 serves as the primary histone chaperone responsible for newly synthesized histone deposition, and it has been established that *cac1*Δ cells exhibit increased OF length in *S. cerevisiae* (*16*). We thus visualized the flap structures of RFs in *cac1*Δ cells (Fig. 4, A to C, and fig. S6, A to C). Our analysis revealed that the inter-flap distance in *cac1*Δ cells clusters around 277 bp (Fig. 4B), noticeably longer than that observed in the WT background in the absence of Cdc9. Analysis of the inter-flap distances less than 300 bp showed that they primarily localized within the 200- to 300-bp range (Fig. 4C). This inter-flap distance distribution is similar to the one

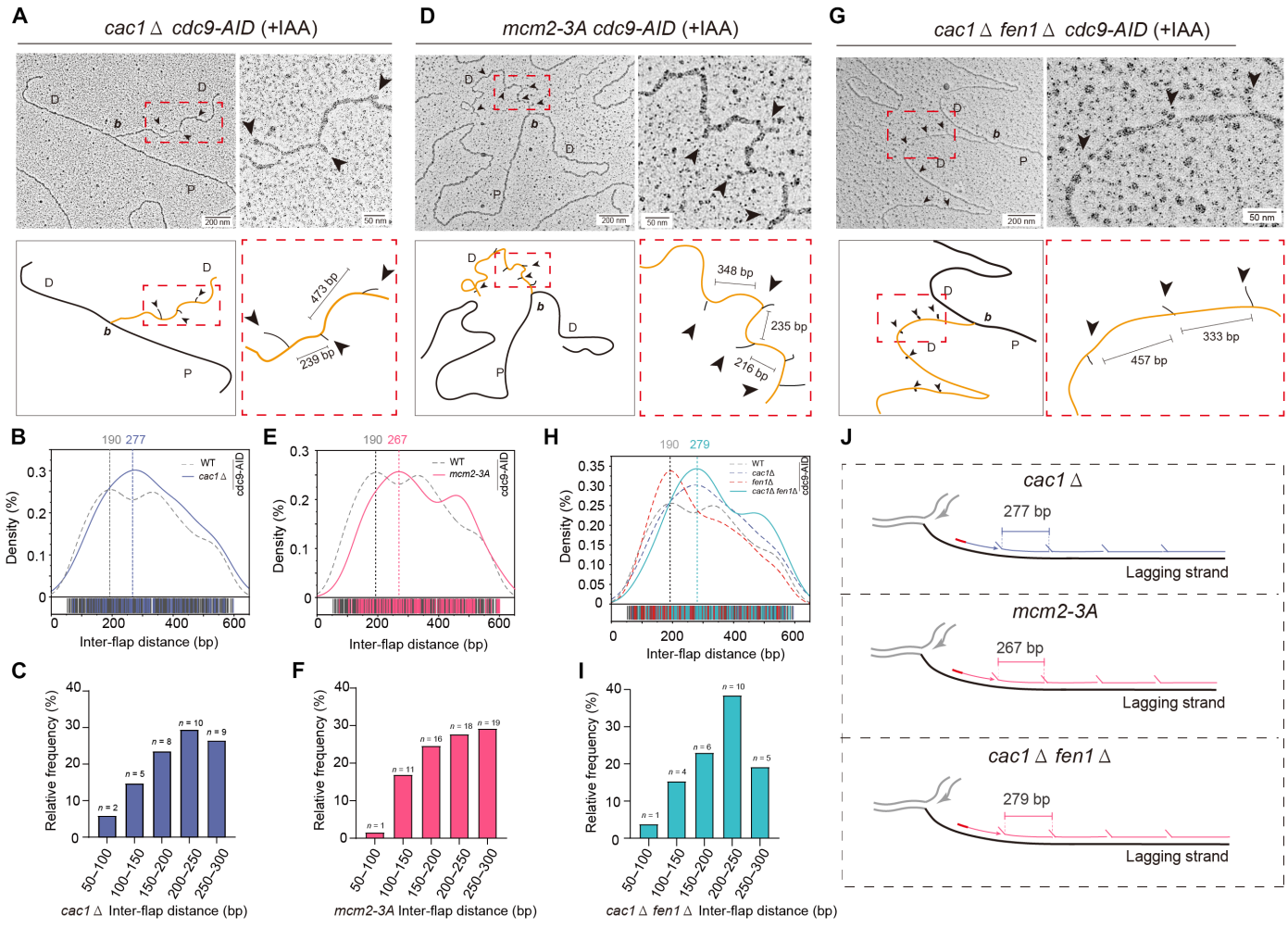

Fig. 4. Impaired nucleosome assembly on lagging strands affects the inter-flap distance. (**A**) Inter-flap distance examples in *cac1*Δ cells RFs. Diagram of the molecule below the image; enlarged view inside the red dashed square to the side. Black arrowheads point to flap DNA, and flap length is labeled. Scale bars, 200 nm (500 bp) and 50 nm (125 bp). (**B**) Probability density fitting of inter-flap distance in *cac1*Δ cells. (**C**) Percentage of inter-flap distance below 300 bp in 50-bp intervals in *cac1*Δ cells. (**D**) Inter-flap distance examples in *mcm2-3A* RFs. Diagram of the molecule below the image; enlarged view inside the red dashed square to the side. Black arrowheads point to flap DNA, and flap length is labeled. Scale bars, 200 nm (500 bp) and 50 nm (125 bp). (**E**) Probability density fitting of inter-flap distance in *mcm2-3A* cells. (**F**) Percentage of inter-flap distance below 300 bp in 50-bp intervals in *mcm2-3A* cells. (**G**) Inter-flap distance examples in *cac1*Δ *fen1*Δ RFs. Diagram of the molecule below the image; enlarged view inside the red dashed square to the side. Black arrowheads point to flap DNA, and flap length is labeled. Scale bars, 200 nm (500 bp) and 50 nm (125 bp). (**H**) Probability density fitting of inter-flap distance in WT, *fen1*Δ, *cac1*Δ, and *cac1*Δ *fen1*Δ cells. (**I**) Percentage of inter-flap distance below 300 bp in 50-bp intervals in *cac1*Δ *fen1*Δ cells. (**J**) Cartoon depicting inter-flap distance in *cac1*Δ, *mcm2-3A*, and *cac1*Δ *fen1*Δ RFs.

observed in *pol32*Δ cells. In addition, the average flap length in *cac1*Δ cells measures around 74 ± 28 nt (fig. S6, J and K), and their distributions predominantly cluster around 43, 59, and 81 nt (fig. S6B), which is close to the one observed in WT. These findings further support the notion that reduced nucleosome occupancy arising from the newly synthesized histone deposition at RF regions influences the OF synthesis, resulting in an increase in the length of OFs.

Mcm2 has previously been found to have a histone-binding domain and is implicated in histone transfer to the lagging strand (*24*, *25*). Studies have demonstrated that the *mcm2-3A* mutation results in a defect in parental histone transfer to the lagging strands (*24*). Therefore, we visualized the flap structures of RFs in *mcm2-3A* cells, too (Fig. 4, D to F, and fig. S6, D to F). Our analysis revealed that the distribution of inter-flap distances ranging from 50 to 600 bp in *mcm2-3A* cells clusters around 267 bp for the first peak (Fig. 4E). In addition, analysis of the inter-flap distances under 300 bp showed that they primarily localized within the 200- to 300-bp range (Fig. 4F), which is noticeably longer than those observed in the WT background in the absence of Cdc9. Furthermore, the flap length in *mcm2-3A* cells measures around 73 ± 34 nt (fig. S6, J and K), and their distributions predominantly cluster around 41, 55, and 77 nt (fig. S6, E and F), which is close to the one observed in WT. These results suggest that reduced nucleosome occupancy arising from parental histone transferring at the lagging strands influences OF synthesis, resulting in an increase the length of OFs.

To rule out the potential effect of the hard-to-detect flaps on the inter-flap distance, we visualized the flap structures of RFs in *cac1*Δ *fen1*Δ cells (Fig. 4, G to I, and fig. S6, G to I). Our analysis revealed that the distribution of inter-flap distances ranging from 50 to 600 bp in *cac1*Δ *fen1*Δ cells clusters around 279 bp for the first peak (Fig. 4H). In addition, analysis of the inter-flap distances under 300 bp showed that they primarily localized within the 200- to 300-bp range (Fig. 4I). These lengths are noticeably similar to the one observed in the *cac1*Δ background in the absence of Cdc9. Furthermore, the flap length in *cac1*Δ *fen1*Δ cells measures around 70 ± 44 nt (fig. S6, J and K), and their distributions predominantly cluster around 47 and 64 nt (fig. S6, H and I), which is similar to that observed in *fen1*Δ cells. Together, these results suggest that nucleosome occupancy, influenced by both newly synthesized histone deposition and parental histone transfer pathways, can influence the length of OFs.

Nucleosome occupancy on nascent chromatin is reduced in cells lacking Pol32

Considering that nucleosome occupancy affects the inter-flap distance, that is, the length of OFs, we asked whether the increased inter-flap distance observed in *pol32*Δ cells is due to reduced nucleosome occupancy. To ask whether the nucleosome occupancy is reduced in *pol32*Δ cells, we measured the nucleosome assembly level on nascent chromatin using the replication-intermediate nucleosome mapping (ReIN-Map) method. Briefly, G_1-phase–arrested yeast cells were released into YPD medium containing bromodeoxyuridine (BrdU) at 25°C for 35 min to allow cells entry into the early S phase with nascent DNA labeled by BrdU (fig. S7A). The resulting chromatin samples were then fragmented by micrococcal nuclease (MNase) to digest DNA between nucleosomes. Nascent nucleosome occupancy was monitored by immunoprecipitation with an antibody against BrdU (BrdU-IP) before strand-specific sequencing (MNase–BrdU-IP–ssSeq). Given that the level of nucleosome occupancy reflects both the capacity for nucleosome assembly and the capacity for DNA synthesis on nascent chromatin, we conducted the analysis in parallel to examine chromatin samples that we fragmented via sonication (sonication–BrdU-IP–seq). This enabled the evaluation of nucleosome assembly capacity based on normalizing the "MNase-seq" dataset with the "sonication-seq" dataset, which provided a "ReIN-Score" for a genome-wide measure of nucleosome occupancy on nascent DNA (Fig. 5A).

The nucleosome occupancy patterns around the transcription start sites (TSSs) were similar among WT, *pol32*Δ, and *pol3*$^{exo-}$ mutant cells at input samples (figs. S7B and S8, A to C), suggesting that neither *pol32*Δ nor *pol3*$^{exo-}$ mutation affects the overall organization of nucleosomes on mature chromatin. We then aligned the MNase–BrdU-IP–enriched fragments to the *S. cerevisiae* genome and observed properly occupied nucleosomes surrounding the autonomously replicating sequence (ARS) consensus sequences (ACSs) in WT early S-phase cells (fig. S7B and Fig. 5C). A slight DNA replication defect was observed in *pol32*Δ cells comparing with WT cells based on the BrdU incorporation level (Fig. 5B). Moreover, a substantial reduction in nucleosome occupancy surrounding ACSs is observed in *pol32*Δ mutant cells (Fig. 5, C, H, and I). This reduction potentially reflects reduced DNA synthesis resulting from sonication–BrdU-IP–seq and compromised nucleosome assembly. To evaluate nucleosome assembly defects in *pol32*Δ mutant cells during DNA synthesis, we normalized MNase–BrdU-IP–seq signals using sonication–BrdU-IP–seq signals to derive a ReIN-Score, which is the quotient of nascent nucleosome coverage based on the MNase–BrdU-IP–seq signal over the nascent DNA coverage represented by the sonication–BrdU-IP–seq signal. The ReIN-Score surrounding ACSs was reduced in *pol32*Δ mutant cells (Fig. 5D). While we detected a mild reduction of nucleosome occupancy surrounding the ACS sites in *pol3*$^{exo-}$ mutant cells based on the MNase–BrdU-IP–seq signals, we did not observe a substantial reduction in the ReIN-Score in the *pol3*$^{exo-}$ mutant cells (Fig. 5, E to G and J). As a control, we did not observe an apparent reduction of nucleosome occupancy surrounding the ACSs in input samples in *pol32*Δ or *pol3*$^{exo-}$ mutant cells (fig. S8, D to F). These results demonstrate that Pol32 is crucial for nucleosome assembly on nascent chromatin.

Pol32 functions to promote nucleosome assembly on the lagging strand

We next separated the sequence reads from the Watson and Crick strands and calculated the average $\log_2$ Watson/Crick ratio for sequence reads at early replication origin sites in the genome of WT yeast cells; this dataset generally reflects the relative extents of DNA synthesis and nucleosome assembly occurring at leading and lagging strands (Fig. 6A). We observed a slight leading-strand bias in the BrdU-IP–ssSeq dataset (Fig. 6A, sonicate–BrdU-IP–ssSeq), supporting that DNA synthesis occurs slightly faster on the leading strand than on the lagging strand. Analysis of our MNase–BrdU-IP–ssSeq dataset revealed a slight leading-strand bias for nucleosome occupancy (Fig. 6, B and I, MNase–BrdU-IP–ssSeq). After performing a normalization to account for the differential strand-specific speed of DNA synthesis, the ReIN-Scores (representing nucleosome assembly capacity) exhibited no apparent bias for either of the daughter strands in WT cells (Fig. 6C, ReIN-Score), suggesting a coordination of nucleosome assembly on both the leading and lagging strands in WT cells.

Compared with WT cells, we did not detect an apparent defect in the coordination of DNA synthesis between the two daughter strands in *pol32*Δ mutant cells or *pol3*$^{exo-}$ mutant cells (Fig. 6, A and E). We observed a marked leading-strand bias in both the MNase–BrdU-IP dataset and the ReIN-Score dataset in *pol32*Δ mutant cells (Fig. 6, C, D, and J) and did not detect an apparent bias in the *pol3*$^{exo-}$ mutant cells (Fig. 6, G, H, and K). Together, these results demonstrate that Pol32 is crucial for nucleosome assembly on the lagging strands.

Pol32 binds histone H3-H4

To investigate how Pol32 functions in nucleosome assembly on the lagging strands, we first tested whether the Pol δ complex can bind histone H3-H4. We first used a bimolecular fluorescence complementation (BiFC) assay to test the Pol δ–H3 interaction in living cells (*26*, *27*). Briefly, either the Pol3 or Pol 32 subunit within the Pol δ complex was tagged with Vc155 (Venus C terminus), while H3 was tagged with Vn173 (Venus N terminus). The fluorescence signal is reconstituted when two nonfluorescent fragments come into proximity due to the interaction between their respective fusion partners. We detected BiFC signals in cells carrying the Pol32-Vc155

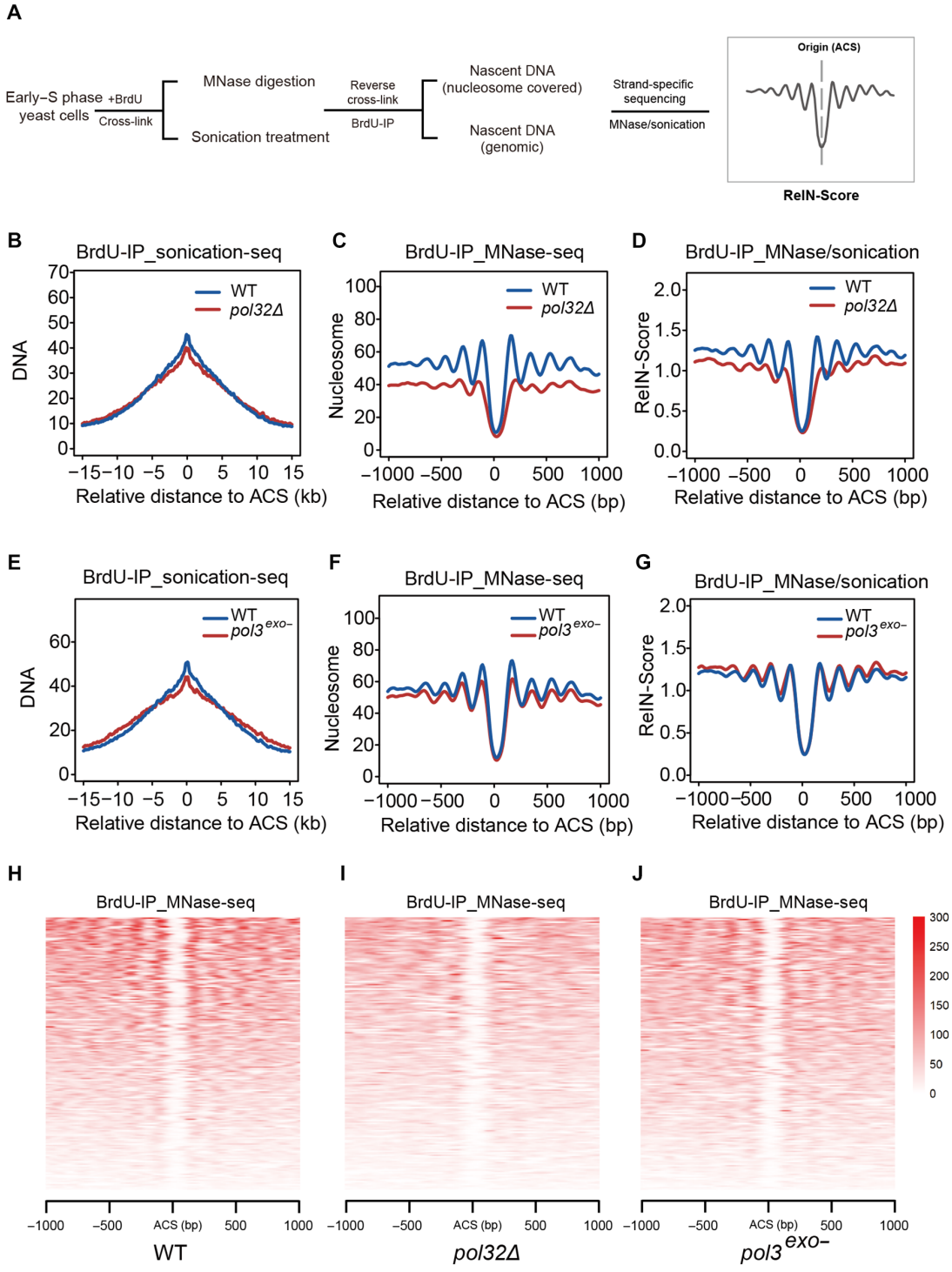

Fig. 5. Nucleosome assembly on nascent chromatin is reduced in *pol32*Δ mutant cells. (**A**) Schematic of ReIN-Map method: Synchronized early–S phase cells were released into the medium with BrdU for 35 min, and chromatin was digested with MNase or sonicated. Samples were treated with BrdU-IP and processed for library construction and sequencing. ReIN-Score was calculated by BrdU-IP MNase/BrdU-IP sonication around ACS. ACS, ARS consensus sequences. (**B**) Average BrdU density around ACS in *pol32*Δ cells from BrdU-IP sonication-seq samples. (**C**) Average nucleosome occupancy around ACS in *pol32*Δcells from BrdU-IP MNase-seq samples. (**D**) ReIN-Score around ACS in *pol32*Δ cells. (**E**) Average BrdU density around ACS in $pol3^{exo-}$ cells from BrdU-IP sonication-seq samples. (**F**) Average nucleosome occupancy around ACS in $pol3^{exo-}$ cells from BrdU-IP MNase-seq samples. (**G**) ReIN-Score around ACS in $pol3^{exo-}$ cells. (**H** to **J**) Heatmap of average nucleosome occupancy around ACS in WT, *pol32*Δ, and $pol3^{exo-}$ cells.

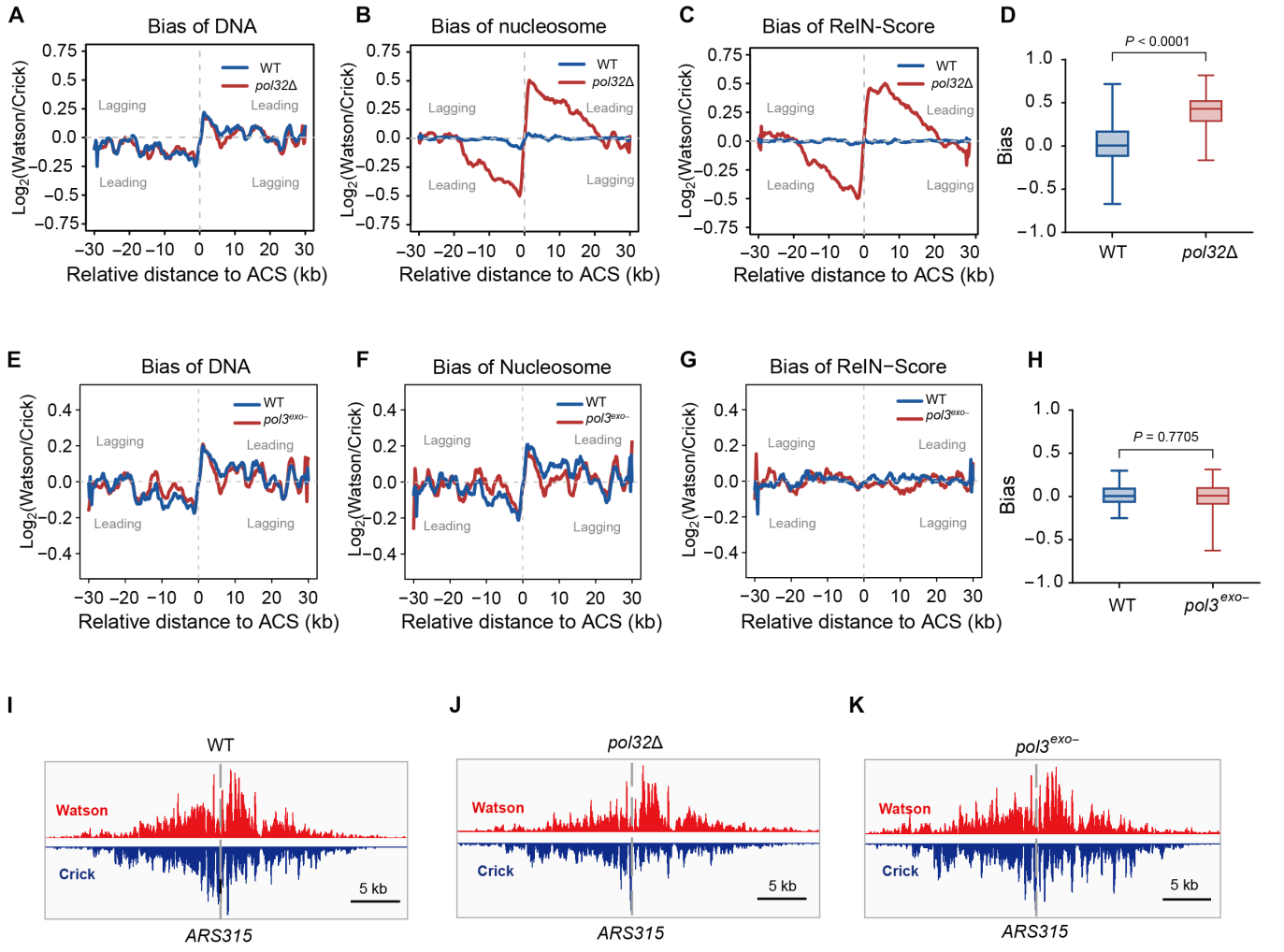

Fig. 6. Nucleosome occupancy is reduced on the lagging strand in *pol32*Δ mutant cells. The bias was calculated by separating the Watson and Crick strand around ACS and calculating $\log_2$(Watson/Crick). (**A**) DNA bias around ACS in *pol32*Δ cells. (**B**) Nucleosome bias around ACS in *pol32*Δ cells. (**C**) ReIN-Score bias around ACS in *pol32*Δ cells. (**D**) Box plots of ReIN-Score bias on leading and lagging strands in WT and *pol32*Δ cells. *P* values from Wilcoxon test. (**E**) DNA bias around ACS in *pol3*$^{exo-}$. (**F**) Nucleosome bias around ACS in *pol3*$^{exo-}$ cells. (**G**) ReIN-Score bias around ACS in *pol3*$^{exo-}$ cells. (**H**) Box plots of ReIN-Score bias on leading and lagging strands in WT and *pol3*$^{exo-}$ cells. *P* values from Wilcoxon test. (**I** to **K**) Snapshots of MNase–BrdU-IP–seq reads surrounding the replication origin *ARS315* in WT, *pol32*Δ, and *pol3*$^{exo-}$ cells.

and H3-Vn173 constructs (Fig. 7A and fig. S9, A and B). However, we did not observe any noticeable signals in cells containing the Pol3-Vc155 and H3-Vn173 constructs (Fig. 7A and fig. S9, A and B). These results indicate that Pol δ interacts with H3-H4 in vivo through the Pol32 subunit.

To further test this idea, the Flag-tagged Pol32 (Pol32-5Flag) complex was purified from yeast cells (Fig. 7B). Both histone H3 and H4 were detected in the Pol32-associated protein complex, indicating that the Pol32 might interact with histones. Next, we conducted in vitro pull-down assays to investigate the direct interaction between Pol32 and histone H3-H4. Recombinant glutathione *S*-transferase (GST)–tagged Pol32 is capable of being directly pulled down with yeast histone H3-H4 in a concentration-dependent manner (Fig. 7, C and D). We then generated truncations for the N terminus (1 to 119 amino acids), middle domain (120 to 243 amino acids), and C terminus (244 to 350 amino acids) of Pol32 fused with GST tags (Fig. 7E). In vitro GST pull-down assays revealed that the C terminus of Pol32 preferentially binds histone H3-H4 (Fig. 7F). Together, these results strongly suggest that the Pol32 subunit of the Pol δ complex binds histone H3-H4 directly and that its C terminus regions are required for its histone binding ability.

To further validate the idea that Pol32-C's histone binding ability functions to the nucleosome assembly on the lagging strands, we first observed the flap structures in *pol32-C*Δ cells (Fig. 8, A to D, and fig. S10). Our analysis revealed that the distribution of inter-flap distances ranging from 50 to 600 bp in *pol32-C*Δ cells clusters around 282 bp for the first peak (Fig. 8B). In addition, analysis of the inter-flap distances under 300 bp showed that they primarily localized within the 250- to 300-bp range (Fig. 8C). These lengths are noticeably similar to the one observed in the *pol32*Δ background in the absence of Cdc9. Furthermore, the flap length in *pol32-C*Δ cells measures around 60 ± 26 nt (fig. S10, A to C), which is similar to that observed in *pol32*Δ cells. The distribution analysis of the flap length ranging from 20 to 90 nt revealed that they are

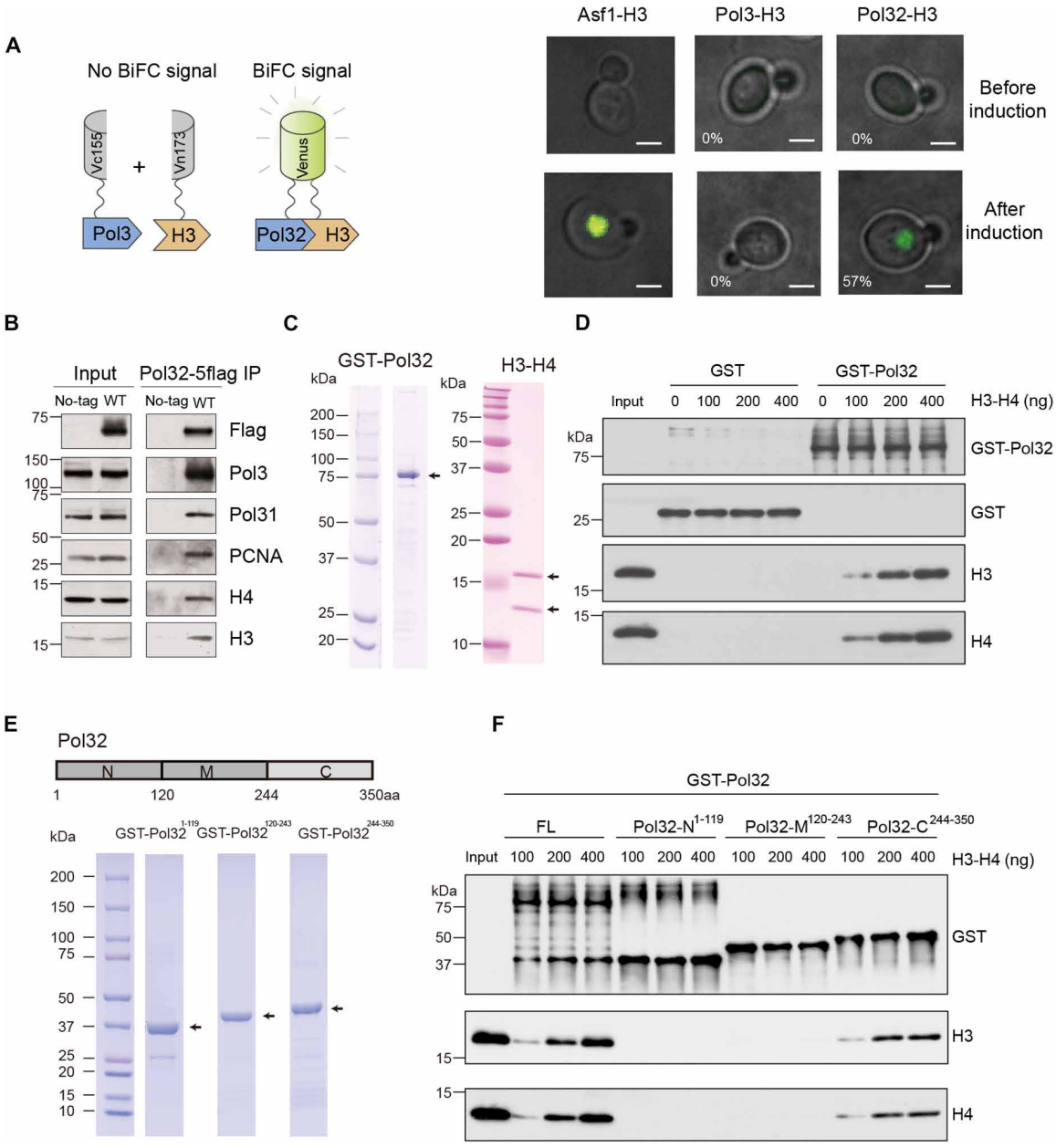

Fig. 7. Pol32 binds histone H3-H4 directly. (**A**) Schematic of the BiFC method: Fluorescence signal is regenerated by the complementation of Venus N terminus (Vn173) and C terminus (Vn155) brought together by their fusion partners' interaction (left). Histone H3 was induced in cells harboring the p426-*GAL1-H3-Vn173* construct with 2% galactose for 3 hours before imaging. BiFC intensity of cells expressing Asf1/Pol3/Pol32-Vc155 and p426-GAL1-H3-Vn173 was observed and quantified (right). Scale bars, 2.5 μm. Results are from at least three independent experiments; one representative experiment is shown. (**B**) Histones co-purified with Pol32. Flag-tagged Pol32 (Pol32-5Flag) was purified from yeast cells and the co-purified proteins were analyzed by Western blot using indicated antibodies. (**C**) Recombinant GST- Pol32 and histone H3-H4 purified from *E. coli* cells, visualized by Coomassie blue staining. (**D**) Pol32 binds histone H3-H4 directly. Recombinant yeast GST-Pol32 was used in in vitro histone pull-down assay and the GST-Pol32–associated proteins were resolved by SDS–polyacrylamide gel electrophoresis (PAGE) and visualized by Western blotting. (**E**) Recombinant truncation forms of GST-Pol32 proteins, GST-Pol32$^{1\text{-}119}$, GST-Pol32$^{120\text{-}243}$ and GST-Pol32$^{244\text{-}350}$ purified from *E. coli* cells and visualized by Coomassie blue staining. (**F**) Pol32$^{244\text{-}350}$ binds histone H3-H4 directly. Recombinant yeast GST-Pol32$^{1\text{-}119}$, GST-Pol32$^{120\text{-}243}$, and GST-Pol32$^{244\text{-}350}$ were used in the in vitro histone pull-down assay. The proteins were resolved by SDS-PAGE and visualized by Western blotting.

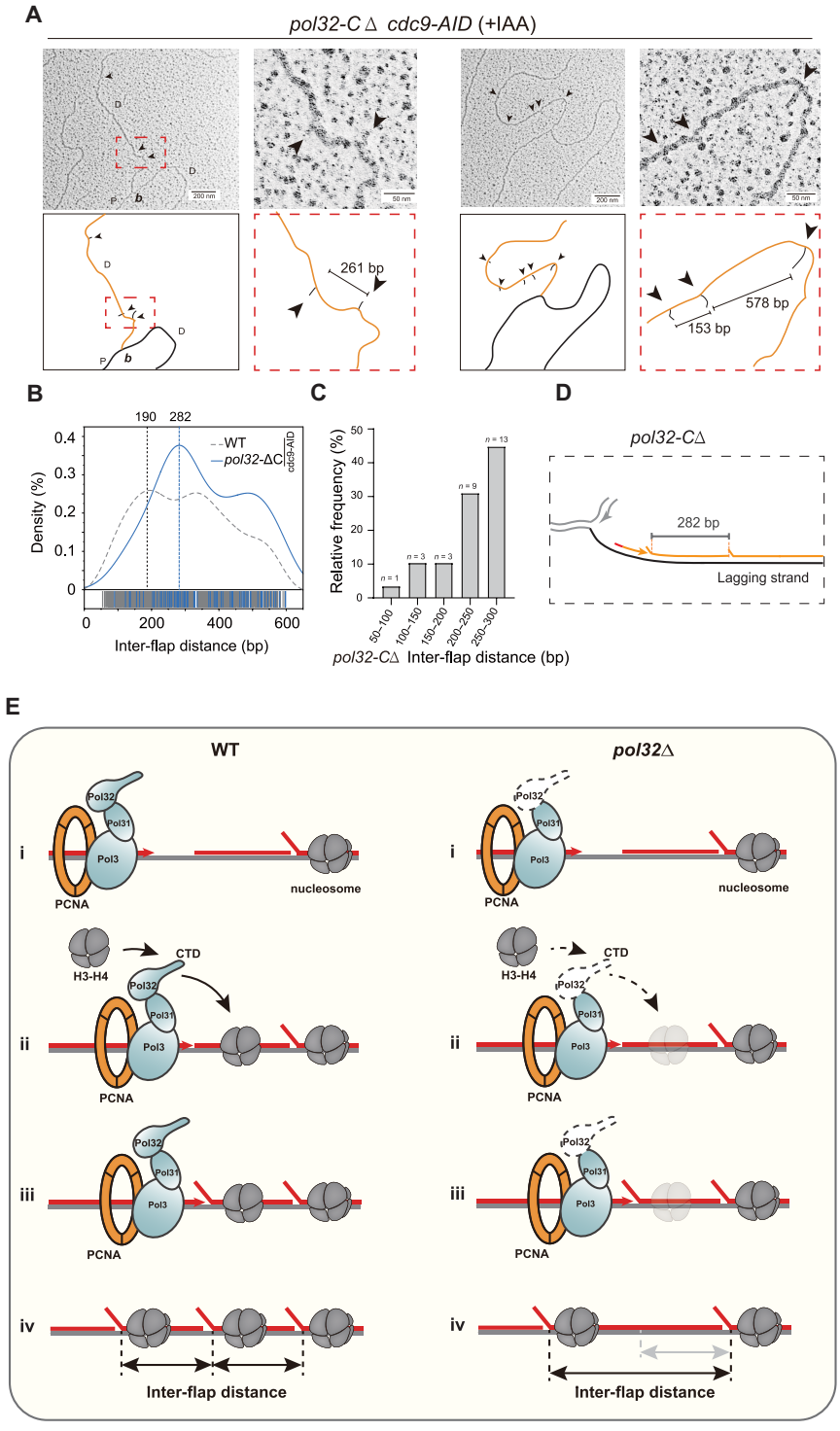

Fig. 8. The C terminus of Pol 32 contributes to nucleosome assembly and regulates the typical OF length. (**A**) Inter-flap distance examples in *pol32-C*Δ RFs. Diagram of the molecule below the image; enlarged view inside the red dashed square to the side. Black arrowheads point to flap DNA, and flap length is labeled. Scale bars, 200 nm (500 bp) and 50 nm (125 bp). (**B**) Probability density fitting of inter-flap distance in *pol32-C*Δ cells. (**C**) Percentage of inter-flap distance below 300 bp in 50-bp intervals in *pol32-C*Δ cells. (**D**) Cartoon depicting inter-flap distance in *pol32-C*Δ cells. (**E**) A model depicting that Pol δ binds histone H3-H4 through its C terminus and couples nucleosome assembly with OF synthesis. (i) Pol δ catalyze the DNA synthesis of the OF; (ii) following OF synthesis, an H3-H4 tetramer is rapidly deposited on the newly synthesized dsDNA fragment by Pol32; (iii) Pol δ can invade the previously generated OF, which has a nascent nucleosome; (iv) a nascent tetramer matures into a complete nucleosome through the addition of H2A/H2B, and repeated cycles of OF synthesis resulting in inter-flap distances that reflect nucleosome size. In *pol32*Δ mutant cells, reduced nucleosome occupancy decreases nucleosome barriers, thereby increasing OF size.

predominantly clustered around 40, 53, and 67 nt, respectively (fig. S10, D and E). This distribution is quite close to the one observed in WT cells, indicating that the deletion of the C terminus in Pol32 might not affect the enzymatic activities mediated by Pol δ in the strand displacement synthesis. These results further support the notion that the C terminus of Pol32 mediates the histone binding ability, which contributes to the nucleosome occupancy on the lagging strands, thus affecting the OF's length.

DISCUSSION

OF synthesis, maturation, and assembly with nucleosomes are rapid, stepwise, and highly coordinated processes. Consequently, observing the intricate stages of OF synthesis and maturation poses notable technical challenges. Motivated by the observation that OFs are enriched under Cdc9 DNA ligase degradation conditions (*15*), we directly observed the distribution of OFs in cells within the Cdc9-AID* background using TEM methods. Upon Cdc9 degradation, we observed the accumulation of flap structures on one daughter strand.

Cdc9, DNA ligase I, is an essential enzyme in budding yeast (*S. cerevisiae*) involved in DNA replication and repair (*18*, *28*). Previous studies showed that, when trinucleotide repeats serve as the lagging strand template, DNA ligase I mutants notably destabilize long repeat tracts, leading to track expansions during DNA replication (*29*). Thus, we should point out that a limitation of this experimental system is that the degradation of Cdc9 affects the OF maturation process. In general, nick translation generates flap structures, followed by flap digestion, and the resulting nick can be ligated by DNA ligase I to complete OF synthesis (*5*). In the absence of Cdc9 DNA ligase I, the failure of ligation may affect flap digestion, resulting in the accumulation of flap structures.

It is important to note that these flap structures characterize the lagging strands, allowing us to analyze the nucleosome assembly process on the OFs. We characterized two parameters of the observed flap structures: flap length, which stems from the lagging strands, and the inter-flap distance between two adjacent flaps. Given the variability in Pt coating, very short flaps may go undetected using electron microscopy (EM). In addition, considering that there might still be low amounts of Cdc9 in cells to catalyze the ligation of OFs, this might affect the calculation of the average inter-flap distance. In this study, we therefore analyzed the distribution of the measured flap-length and inter-flap distance, instead of simply calculating the averages. We observed that the inter-flap distance clustered around two peaks, with 190 bp as the major peaks in WT cells under Cdc9 degradation. Given that the 190 bp is close to the size of a typical OF in WT, these results suggest that, despite the technical limitations in this experimental system, the extensive number of RFs observed and comprehensive analysis still provide valuable information about OFs.

The observed flap structures are influenced by both strand displacement activities and nuclease digestion events

Previous studies based on genome-wide sequencing methods have revealed that, in the absence of DNA ligase I Cdc9, the position of the 5′ termini of OFs shifts compared to the nucleosome dyad position during the S phase. Within 30 min of release into the S phase, it is observed that the 5′ ends of OFs shift ~50 bp away from the nucleosome dyad position (*17*). Supporting this notion, we observed such flap structures in replication products within a Cdc9 degradation background under an electron microscope. Measurement of these flaps indicated an average length of around 69 ± 27 nt. Similar lengths were also observed in *S. pombe* fission yeast cells (*12*). Despite the potential for ligation events to still occur under conditions of Cdc9 degradation and the challenge in detecting very short flap structures, we noted that these flap structures in the early S phase (S35) from the branching points to more than 5 kb away, with the highest frequency observed close to the branching points. Combining observations from later time points and mutant backgrounds, the flap structures appear to be relatively stable within the timeframe that we studied.

Of note, we analyzed the length distribution ranging from 20 to 90 nt of the observed flaps and identified clusters at ~39, 52, and 67 nt in the early–S phase (S35) WT background, suggesting that the generated flap length can be dynamic. The 5′ end of OFs can move from upstream toward the nucleosome dyad position at later time points in the S phase under Cdc9-degradation conditions (*17*). Consistent with this observation, at the early time point, S35, the major peak was centered around 52 nt. At the later time point, S50, during the S phase, the major peak shifted to around 39 nt, which is shorter than the peak observed at the early time point.

Despite technological challenges in measuring the length of the ssDNA, the substantial sample size that we analyzed enabled us to detect a potential interval of about 13 to 15 nt between these flaps. In a typical nucleosome core particle, there are defined superhelical locations (SHLs) that help describe the positioning of DNA as it wraps around the histone octamer. Of the 147-bp DNA wrapped around the histone octamers, 14 distinct sites of contact are observed (*22*). Given the potential barrier posed by nucleosome in strand displacement synthesis, the observed interval may be related to the SHL positions and the interactions between histones and DNA within a nucleosome structure. Supportively, in *pol3*$^{exo-}$ mutant cells (with enhanced strand displacement activity), each peak of the clustered flap lengths increased by ~13 nt, suggesting a link between nucleosome structure and Pol δ's strand displacement activity. It would be interesting to determine that in future studies.

It was reported that, in *Schizosaccharomyces pombe*, while flap structures can also be observed on replication intermediates, their frequency is much lower than what we observed under Cdc9-depletion conditions (*12*). The frequency of observed flap structures increases in backgrounds where nucleases involved in flap processing are mutated (*12*). Prior studies have shown that the strand displacement activity of Pol δ contributes to the generation of flap structures, which facilitates subsequent DNA ligation steps (*4*, *30*–*32*). Moreover, Fen1, also referred to as Flap Endonuclease 1, primarily functions to process and remove short flaps in DNA, typically handling single-nucleotide flaps (*33*). The 1-nt double-flap structure is the preferred substrate for eukaryotic Fen1 in vitro (*34*, *35*). When excessive strand replacement occurs, the resulting longer ssDNA is wrapped in RPA, which inhibits Fen1 from processing but favors Dna2 cleavage (*10*). This dynamic balance between strand displacement and flap cutting leads to longer flap lengths in vivo. Comparing the flap lengths in Pol δ mutant cells (*pol3*$^{exo-}$ and *pol32*Δ) and nuclease mutant cells (*fen1*Δ) with those in WT cells, we detected significant changes, supporting the idea that both strand displacement activity and nuclease digestion affect flap lengths.

The flap lengths in RC nucleosome assembly–defective mutant cells (*cac1*Δ and *mcm2-3A*) remain relatively similar to those in WT cells. Consistent with this idea, the distribution of flap lengths in *pol32-C*Δ mutant cells is similar to those in WT cells. Furthermore,

the distribution of flap lengths in *cac1*Δ *fen1*Δ double-mutant cells is quite similar to that observed in *fen1*Δ cells. These results suggest that the flap lengths in cells are quite dynamic, influenced by both strand displacement activity and nuclease digestion steps.

Pol32 binds histone H3-H4 and functions in histone dynamics at the lagging strands

In the context of the chromatin environment, the newly synthesized OFs need to be rapidly wrapped with histones to form nucleosomes. It has been established that nucleosomes posed barriers to Pol δ–catalyzed strand displacement activity (*15*, *36*). Supporting this notion, we observed that the average distance between adjacent flap structures, the inter-flap distance, is about 190 bp in WT cells under Cdc9 degradation and reflects a typical matured OF size, which agrees well with the nucleosome size. By comparing samples from early and later time points in the S phase, we found that the inter-flap distance remains relatively stable. Moreover, mutations in *pol3*$^{exo-}$ or *fen1*Δ do not affect the first peak of the inter-flap distance, suggesting that the enhanced strand displacement activity or flap digestion process does not affect the typical matured OF size. Unexpectedly, we discovered that the inter-flap distance is significantly changed in *pol32*Δ cells and that an inter-flap distance peak clustering around 280 bp was detected.

In the budding yeast *S. cerevisiae*, the Pol δ complex is a heterotrimeric complex, which comprises three subunits: the essential catalytic subunit, Pol3, along with two accessory subunits Pol31 and Pol32 (*2*, *37*). While Pol31 is essential for viability, Pol32 is not in the budding yeast (*38*). It was reported that Pol32 is required for strand displacement activity and that deletion of Pol32 results in a reduced strand displacement (*8*). It is possible that, in the absence of Pol32, the resulting flaps may exhibit significant shortening. Consequently, these truncated flaps could become more susceptible to cleavage by Fen1 at their bases, rendering them undetectable. As a result, an increased inter-flap distance may become apparent. If this is true, then one would expect that, in *pol32*Δ *fen1*Δ double-mutant cells, the inter-flap distance would be restored to normal. We found that this double-mutant cell is lethal (fig. S5), indicating the essential role of Fen1 in *pol32*Δ cells.

However, if this were the sole explanation for the increased inter-flap distance in the *pol32*Δ background, then one would expect to observe a clustered peak resembling a WT pattern but in a di-OF size when analyzing the distribution of inter-flap distances, given the large numbers that we measured. However, the 280-bp peak observed in *pol32*Δ cells is clearly bigger than the mono-OF size and shorter than the typical di-OF size. On the basis of the clustered peak patterns we observed in *pol32*Δ cells, considering that it was established that the nucleosome assembly level affects the OF length (*15*), we, therefore, hypothesize that Pol32 has a role in nucleosome assembly.

This hypothesis is supported by our observations that the inter-flap distance is primarily influenced by nucleosome assembly events. We found that the clustered inter-flap distance peaks at 277 bp in *cac1*Δ cells and 267 bp in *mcm2-3A* cells (Fig. 4), which represent defects in newly synthesized and old histone deposition, respectively. These inter-flap distances are consistent with that observed in *pol32*Δ cells. Consistent with this idea, Pol32 directly binds histone H3-H4, and its C terminus is crucial for this binding. Consequently, we observed a significant decrease in nucleosome occupancy at the lagging strand on nascent chromatin in *pol32*Δ cells. Reduced nucleosome occupancy decreases nucleosome barriers, thereby increasing OF size (Fig. 8E). These findings strongly suggest that the Pol32 subunit in the Pol δ complex plays a role in histone binding, facilitating the transfer of parental histones to the nascent strands.

Recently, it was reported that several replisome components have histone-binding abilities and function in parental histone recycling and transfer. For instance, both Mcm2 in the Mcm2-7 helicase and the Pol1 subunit in the Pol α complex have histone binding motifs that facilitate the transfer of parental histones along the Mcm2–Ctf4–Pol α axis (*24*). Moreover, the Dpb3-Dpb4 subunits in the Pol ε complex can directly bind histone H3-H4 and contribute to parental histone transfer to the leading strand (*39*). Our research revealed that Pol32 binds histone H3-H4 and contributes to nucleosome assembly on lagging strands, providing a novel mechanism for replisome components to engage in histone dynamics. Recent structural studies of the Pol δ complex suggested that the Pol32 subunit localizes slightly apart from the Pol3 subunit. It interacts with the Pol31 subunit via its N terminus, while its C terminus is positioned at the front of the Pol δ complex. Although direct binding of the Pol32-PCNA-interacting protein (PIP) box to proliferating cell nuclear antigen (PCNA) has not been confirmed, the Pol32-Pol31 subunit extension from the Pol δ complex forms a hook directed toward PCNA (*37*). We propose that this structural feature allows Pol32 to bind histone H3-H4 and allow the loading of H3-H4 onto the newly synthesized double-stranded DNA (dsDNA). We found that the C terminus of Pol32 is crucial for Pol32 to bind histone H3-H4. In addition, Pol32 has been shown to interact with Pol α-primase (*23*). This interaction potentially extends the Mcm2–Ctf4–Pol α axis into the Ctf4–Pol α–Pol32 axis, ensuring parental histone transfer to the terminus site, the newly synthesized dsDNA.

MATERIALS AND METHODS

Strains and cultural conditions

Standard yeast medium and genetic techniques were used. All yeast strains were derived from W303-1A background (*MATa ade2-1 ura3-1 his3-11,15 trp1-1 leu2-3,112 can1-100*) (*40*). The BrdU incorporation strains are derived from Cvy61 and Cvy63 (*41*). The cells with Cdc9-AID* tag were incubated in yeast culture (YPD) at 30°C to optical density at 600 nm (OD_{600}) of 0.4 to 0.5, and, then, the cells were arrested in the G_1 phase using α-factor, during which time degradation of the Cdc9 was stimulated by activation of the degron system using IAA. Then, the cells were released into the YPD culture with IAA into the S phase for 35 min at 25°C.

Preparation of replication intermediate DNA for TEM

The replication intermediates DNA were purified and enriched as previously described (*42*). Briefly, early–S phase cells were cross-linked with trioxsalen (final concentration of 10 μg/ml). Total DNA was isolated and digested with *Pvu* I. Replication intermediates were enriched with benzoylated naphthoylated diethylaminoethyl (BND) cellulose and spread in a monolayer of BAC on the surface of bidistilled water for electron microscopic examination (*42*, *43*).

In vivo psoralen cross-linking

Preparation of replication intermediates was performed as described previously (*42*). Samples are typically collected at 25°C for 35 min during synchronization experiments, with each sample containing between 2×10^9 and 5×10^9 cells (200 ml of culture at 1×10^7 to $2.5 \times$

10^7 cells/ml). Spin the cells down at 3200*g* for 10 min, resuspend them in ice-cold water, and transfer the suspension to 50-ml tubes. Spin again at 3200*g* for 5 min at 4°C. Resuspend the pellet in 20 ml of ice-cold water and transfer the cells into an 8.5-cm-diameter petri dish. To simultaneously cross-link several samples, install five 365-nm monochromatic lamps in the cross-linker, making sure that each is properly inserted and lights up upon starting the device. Add 1 ml of trimethylpsoralen (TMP) stock solution (to achieve a final concentration of 10 μg/ml) to the cell suspension in a petri dish and mix thoroughly with a pipette. Incubate for 5 min in the dark on a precooled metal support and then place the support with the petri dishes on a freezing pack and irradiate for 3 min. Transfer the cell suspension to a 50-ml tube and keep it on ice. Wash the dish twice with 1 ml of water to collect any remaining cells, pooling the washes in the same 50-ml tube. Centrifuge the cells at 3200*g* for 10 min and use the pellet for DNA extraction.

Genomic DNA extraction by cetyltrimethylammonium bromide (CTAB) method

Resuspend the cells in 5 ml of spheroplasting buffer and incubate at 30°C for 45 min, inverting the tube several times during the process. After incubation, centrifuge the spheroplasts at 6000*g* for 10 min. Resuspend the spheroplasts in 2 ml of distilled water and then quickly add 2.5 ml of solution I and 200 μl of ribonuclease (RNase) A (10 mg/ml). Incubate this mixture at 50°C for 30 min, then add 200 μl of proteinase K (20 mg/ml), and gently mix. Continue incubation for 1.5 to 2 hours at 50°C, inverting the tube occasionally. Ensure that the solution becomes clear, breaking any clumps with precut 1-ml tips if necessary. If clumps persist after 2 hours, then add an additional 100 μl of proteinase K (20 mg/ml) and incubate overnight at 30°C.

Centrifuge at 3200*g* for 10 min and retain the pellet for further processing. Carefully transfer the supernatant to a 15-ml tube containing 2.5 ml of chloroform/isoamyl alcohol 24:1 at room temperature (RT), mixing by inverting several times. After spinning at RT at 3200*g* for 10 min, remove the clear upper phase, avoiding the white protein layer, and transfer it to a 30-ml Kimble glass tube. Gently add 10 ml of solution II, cover with parafilm, and invert several times until the solution becomes turbid. Allow it to sit at RT for 10 to 15 min until turbidity is detectable. Centrifuge at 12,000*g* for 10 min, discard the supernatant, and dissolve the pellet completely in 2 ml of solution III by briefly heating at 37°C.

Resuspend the pellet vigorously in 2 ml of solution III and incubate at 50°C for 1 hour, using precut 200-μl tips to aid in resuspension. Ensure that the solution is homogeneous before transferring it to a 15 ml tube containing 1 ml of chloroform/isoamyl alcohol 24:1 at RT. Mix by inverting and spin at RT at 3200*g* for 10 min. Carefully transfer 2 ml of the clear upper phase to the Kimble glass tube for a final volume of 4 ml. Add 4 ml of isopropanol to precipitate the DNA, mix gently, and centrifuge at 12,000*g* for 10 min.

Discard the supernatant and wash the DNA pellet with 1 ml of 70% ethanol at RT. Remove as much ethanol as possible and briefly spin to collect residual ethanol at the bottom of the tube. Remove the remaining ethanol with a 200-μl pipette and then dry the pellet by briefly incubating the open Kimble glass tube in a 37°C water bath. Resuspend the dried pellet in 200 μl of 1× Tris-EDTA Buffer (TE), cover with parafilm and incubate for 30 min at 37°C (or overnight at RT) to ensure thorough resuspension. Briefly spin down and transfer the DNA solution to a microfuge tube using a precut 200-μl tip to avoid shearing the genomic DNA. Assess the quality and concentration of the DNA, as well as possible RNA contamination, by agarose gel electrophoresis. Typically, the yield from 4×10^9 to 1×10^{10} cells is 10 to 60 μg of genomic DNA per sample.

Digestion and enrichment of replication intermediates

Digest 10 to 15 μg of genomic DNA from yeast cells with 50 to 100 U of Pvu I restriction enzyme in the appropriate buffer for 3 to 5 hours at 37°C. If the DNA preparations are diluted, then increase the reaction volume from the standard 250 μl as needed. Add small amounts of the appropriate RNase enzymes if necessary.

For chromatography, pour 1 ml of BND cellulose stock into a column with its bottom cut to facilitate gravity flow. Wash the column six times with 1 ml of 10 mM tris-HCl (pH 8.0) and 1 M NaCl, ensuring complete flow before each subsequent wash. Equilibrate the column six times with 1 ml of 10 mM tris-HCl (pH 8) and 300 mM NaCl, again allowing for full flow each time. Adjust the restriction digest to a final concentration of 300 mM NaCl using 5 M NaCl stock and then bring the total volume to 600 μl with 10 mM tris-HCl (pH 8) and 300 mM NaCl. Seal the bottom of the column, load the pre-equilibrated digestion mix, and incubate for 30 min at RT, resuspending the BND resin every 10 min. After incubation, remove the cap to enable gravity flow, collecting the effluent in a 2-ml microfuge tube—this contains primarily linear dsDNA molecules (70 to 95% of total DNA). Wash the column twice with 1 ml of 10 mM tris-HCl (pH 8.0) and 1 M NaCl, allowing for complete drainage after each wash. Reseal the column and add 600 μl of 10 mM tris-HCl (pH 8), 1 M NaCl, and 1.8% caffeine, incubating for another 10 min at RT to elute remaining DNA molecules, gently resuspending after 5 min. Collect the flow-through, which is enriched in replication intermediates.

Purify the DNA using an Amicon size exclusion column: load the 600 μl of eluate, spin for 5 min at 2400*g*, and wash the membrane twice with 200 μl of 1× TE, spinning for 3 min at 10,000*g* after each wash. Continue to spin for 10 min at 10,000*g* until only 10 to 30 μl remain. Transfer the sample to a fresh tube per the manufacturer's instructions. Assess DNA quality and concentration with a 1-μl aliquot on an agarose gel. If necessary, adjust the final volume by adding 1× TE or concentrate the sample using a standard vacuum evaporator to achieve an optimal DNA concentration of 10 to 50 ng/μl.

To observe flap structures in the forks, high-resolution EM images are acquired. No supporting film was placed under the carbon film. The nucleic acids on the carbon film were stained with uranyl acetate. The thickness of the platinum film was 7.5 to 7.8 nm. The angle for DNA shadowing with platinum was 7.5° (*12*). Flap lengths were measured by comparing them to the M13 ssDNA EM image, while the length of dsDNA was assessed using both the pRS313 dsDNA EM image and M13 ssDNA. Electron micrographs were captured at ×140,000 magnification and an accelerating voltage of 120 kV using an FEI Tecnai 20. At least two independent experiments were performed to collect each sample. A paired Student's *t* test was used to calculate the *P* value [not significant (n.s.), $*0.01 < P \leq 0.05$, $**0.001 < P \leq 0.01$].

Flag-tagged protein purification

Yeast cells were harvested and resuspended in Flag-IP buffer [50 mM Hepes (pH 7.5), 150 mM NaCl, 6 mM $MgCl_2$, 1 mM EDTA, 0.2% NP-40, 1 mM phenylmethylsulfonyl fluoride (PMSF), and 1 mM

dithiothreitol] containing 1 mM PMSF (Sigma-Aldrich, P7626), 1 mM Pefabloc (Roche, 11429876001), and 1 mM benzamidine (Sigma-Aldrich, B6506). The resuspended yeast cells were pulverized in the Freezer/Mill grinder (SPEX). The cell lysate was centrifugated at 20,450*g*, and the supernatant was incubated with ANTI-FLAG M2 Affinity Gel (Sigma-Aldrich, A2220) for 2 hours at 4°C. The beads were washed three times and then eluted with 3× FLAG tag peptide (1 mg/ml; Chinese peptide 805779). The elution was concentrated by 25% trichloroacetic acid (Sigma-Aldrich, T9159) precipitation.

Immunoblotting

The samples were resuspended in SDS buffer, boiled at 100°C for 3 min, and resolved on homemade 8% or 15% SDS–polyacrylamide gel electrophoresis (PAGE) gels at 120 V for 90 min. The proteins were then transferred to the nitrocellulose membrane (GE Healthcare, 10600002) at 0.25 A for 90 min. The membranes were probed with antibodies against Pol3 (homemade), Pol31 (homemade), PCNA (a gift from Z. Zhang's lab), histone H3 (Abcam, ab1791), histone H4 (EASYBIO, BE3194), H3K4me3 (Abcam, ab8580), and Flag tag (Sigma-Aldrich, F1804).

ReIN-Map assay

The ReIN-Map assay was performed as previously described (*44*). Yeast was treated by α-factor and was arrested in the G_1 phase. Then, yeast was released into a fresh YPD medium containing BrdU for 35 min. Cells in the G_1 phase (0 min) and the early S phase (35 min) were collected for the following experiments. Half of the cells were treated with zymolase first and then with MNase to obtain the mononucleosome-covered DNA. The other half was lysed by bead beating, and the DNA was sonicated to be fragmented. Both samples were reverse cross-linked, and the DNA was purified. BrdU-labeled DNA was enriched by immunoprecipitation (BrdU-IP) with BrdU antibodies. The resulted DNA samples were then used for ssDNA libraries construction and subjected for Illumina sequencing.

Sequencing and data analysis

The sequencing results were used to calculate ReIN-Score and bias as previously described (*45*). Briefly, the ssDNA libraries were sequenced using the Illumina NovaSeq 6000 system. The paired-end sequence data underwent quality control, and reads were aligned to the yeast genome reference sacCer3 using Bowtie2. Subsequently, we identified BrdU-enriched regions using MACS2. We used DANPOS (v2.2.2) to calculate BrdU-enriched regions and nucleosome positions. Nucleosome scores and DNA scores were derived from MNase–BrdU-IP–seq and sonication–BrdU-IP–seq datasets, respectively. Nucleosome or DNA scores represent BrdU-positive signals normalized by the background noise. Normalization of nucleosome and DNA scores involved subtracting the signal expected from the BrdU-positive region (considered as downstream and upstream 2 kb of the BrdU-enriched region), representing background noise, which was then normalized to 1 per base for all samples. Then, the nucleosome and DNA around ACS and TSS were collected and calculated to ReIN-Score (MNase–BrdU-IP–seq/sonication–BrdU-IP–seq). The Watson and crick strand were divided and collected around ACS. Then, the bias of ReIN-Score was calculated by $\log_2$(Watson/Crick). A Wilcoxon matched-pairs signed-rank test was used to calculate the *P* value.

BiFC assay

The BiFC assay was performed as previously described (*46*) using split YFP. Vc155 was fused to Pol32, and Vn173 was fused to histone H3 driven by a GAL1 promoter in the p426-GAL1-URA3 plasmid, with which yeast cells were transformed. Cells were cultured to OD_{600} of 0.4 in synthetic complete uracil-dropout medium (SCM-URA) medium, induced by 2% galactose for 3 hours at 25°C, washed in water, and subsequently resuspended in phosphate-buffered saline. Resuspended samples were spread on a petri dish and covered with 1% agarose gel. Images were captured using an Andor Dragonfly High-Speed Confocal Microscope system (Andor Dragonfly 200) with a 514-nm laser to excite fluorescence, which was collected by a Fusion acquisition system and quantitated using the ImageJ software. The quantitated results were from three independent experiments. An unpaired Student's *t* test was used to calculate the *P* value (n.s., *$0.01 < P \leq 0.05$, **$0.001 < P \leq 0.01$).

Protein purification and in vitro pull-down assay

Purification of recombinant *S. cerevisiae* H3-H4 was performed as described (*47*). Full-length *S. cerevisiae* Pol32 was cloned into the pGEX-4 T-1 vector, and GST-Pol32 was expressed in the BL21(DE3) strain of *Escherichia coli*. The purification of GST-tagged protein was performed as previously described (*48*). In vitro pull-down assays were performed as described with minor modifications (*45*). Briefly, GST or GST-Pol32 (5 μg) was bound to glutathione-Sepharose resin, incubated with histone H3-H4 overnight in buffer A150 [25 mM tris (pH 7.5), 1 mM EDTA, 0.01% NP-40, and 150 mM NaCl] at 4°C, and then washed three times with A150 extensively. The bounded proteins were eluted with SDS-PAGE sample buffer and detected by Western blot using indicated antibodies.

Supplementary Materials

This PDF file includes:

Figs. S1 to S10
Tables S1 to S4

REFERENCES AND NOTES

1. K. D. Zhou, G. Gaullier, K. Luger, Nucleosome structure and dynamics are coming of age. *Nat. Struct. Mol. Biol.* **26**, 3–13 (2019).
2. P. M. J. Burgers, T. A. Kunkel, Eukaryotic DNA replication fork. *Annu. Rev. Biochem.* **86**, 417–438 (2017).
3. P. M. J. Burgers, Polymerase dynamics at the eukaryotic DNA replication fork. *J. Biol. Chem.* **284**, 4041–4045 (2009).
4. L. Zheng, B. H. Shen, Okazaki fragment maturation: Nucleases take centre stage. *J. Mol. Cell Biol.* **3**, 23–30 (2011).
5. L. Balakrishnan, R. A. Bambara, Okazaki fragment metabolism. *Cold Spring Harb. Perspect. Biol.* **5**, a010173 (2013).
6. S. Waga, G. J. Hannon, D. Beach, B. Stillman, The p21 inhibitor of cyclin-dependent kinases controls DNA replication by interaction with PCNA. *Nature* **369**, 574–578 (1994).
7. P. Garg, P. M. J. Burgers, DNA polymerases that propagate the eukaryotic DNA replication fork. *Crit. Rev. Biochem. Mol. Biol.* **40**, 115–128 (2005).
8. C. M. Stith, J. Sterling, M. A. Resnick, D. A. Gordenin, P. M. Burgers, Flexibility of eukaryotic Okazaki fragment maturation through regulated strand displacement synthesis. *J. Biol. Chem.* **283**, 34129–34140 (2008).
9. Y. I. Pavlov, C. Frahm, S. A. N. McElhinny, A. Niimi, M. Suzuki, T. A. Kunkel, Evidence that errors made by DNA polymerase α are corrected by DNA polymerase δ. *Curr. Biol.* **16**, 202–207 (2006).
10. H. I. Kao, J. Veeraraghavan, P. Polaczek, J. L. Campbell, R. A. Bambara, On the roles of *Saccharomyces cerevisiae* Dna2p and flap endonuclease 1 in Okazaki fragment processing. *J. Biol. Chem.* **279**, 15014–15024 (2004).
11. R. Ayyagari, X. V. Gomes, D. A. Gordenin, P. M. J. Burgers, Okazaki fragment maturation in yeast. I. Distribution of functions between FEN1 AND DNA2. *J. Biol. Chem.* **278**, 1618–1625 (2003).

12. B. C. Liu, J. Z. Hu, J. N. Wang, D. C. Kong, Direct visualization of RNA-DNA primer removal from okazaki fragments provides support for flap cleavage and exonucleolytic pathways in eukaryotic cells. *J. Biol. Chem.* **292**, 4777–4788 (2017).
13. D. M. MacAlpine, G. Almouzni, Chromatin and DNA replication. *Cold Spring Harb. Perspect. Biol.* **5**, a010207 (2013).
14. G. Almouzni, D. J. Clark, M. Mechali, A. P. Wolffe, Chromatin assembly on replicating DNA in vitro. *Nucleic Acids Res.* **18**, 5767–5774 (1990).
15. D. J. Smith, I. Whitehouse, Intrinsic coupling of lagging-strand synthesis to chromatin assembly. *Nature* **483**, 434–438 (2012).
16. T. Yadav, I. Whitehouse, Replication-coupled nucleosome assembly and positioning by ATP-dependent chromatin-remodeling enzymes. *Cell Rep.* **15**, 715–723 (2016).
17. N. C. Koussa, D. J. Smith, Post-replicative nick translation occurs on the lagging strand during prolonged depletion of DNA ligase I in *Saccharomyces cerevisiae*. *G3* **11**, jkab205 (2021).
18. L. H. Johnston, K. A. Nasmyth, *Saccharomyces cerevisiae* cell cycle mutant cdc9 is defective in DNA ligase. *Nature* **274**, 891–893 (1978).
19. T. A. Peterson, L. Prakash, S. Prakash, M. A. Osley, S. I. Reed, Regulation of CDC9, the *Saccharomyces cerevisiae* gene that encodes DNA ligase. *Mol. Cell. Biol.* **5**, 226–235 (1985).
20. M. Morawska, H. D. Ulrich, An expanded tool kit for the auxin-inducible degron system in budding yeast. *Yeast* **30**, 341–351 (2013).
21. J. M. Sogo, H. Stahl, T. Koller, R. Knippers, Structure of replicating simian virus 40 minichromosomes. The replication fork, core histone segregation and terminal structures. *J. Mol. Biol.* **189**, 189–204 (1986).
22. K. Luger, A. W. Mäder, R. K. Richmond, D. F. Sargent, T. J. Richmond, Crystal structure of the nucleosome core particle at 2.8 A resolution. *Nature* **389**, 251–260 (1997).
23. E. Johansson, P. Garg, P. M. J. Burgers, The pol32 subunit of DNA polymerase δ contains separable domains for processive replication and proliferating cell nuclear antigen (PCNA) binding. *J. Biol. Chem.* **279**, 1907–1915 (2004).
24. H. Y. Gan, A. Serra-Cardona, X. Hua, H. Zhou, K. Labib, C. Yu, Z. Zhang, The Mcm2-Ctf4-Polα axis facilitates parental histone H3-H4 transfer to lagging strands. *Mol. Cell* **72**, 140–151.e3 (2018).
25. N. Petryk, M. Dalby, A. Wenger, C. B. Stromme, A. Strandsby, R. Andersson, A. Groth, MCM2 promotes symmetric inheritance of modified histones during DNA replication. *Science* **361**, 1389–1392 (2018).
26. Y. J. Shyu, C. D. Suarez, C. D. Hu, Visualization of ternary complexes in living cells by using a BiFC-based FRET assay. *Nat. Protoc.* **3**, 1693–1702 (2008).
27. S. Wang, M. Ding, B. X. Xue, Y. P. Hou, Y. J. Sun, Live cell visualization of multiple protein-protein interactions with BiFC rainbow. *ACS Chem. Biol.* **13**, 1180–1188 (2018).
28. L. Prakash, S. Prakash, Isolation and characterization of MMS-sensitive mutants of *Saccharomyces cerevisiae*. *Genetics* **86**, 33–55 (1977).
29. E. W. Refsland, D. M. Livingston, Interactions among DNA ligase I, the flap endonuclease and proliferating cell nuclear antigen in the expansion and contraction of CAG repeat tracts in yeast. *Genetics* **171**, 923–934 (2005).
30. Y. H. Jin, R. Obert, P. M. J. Burgers, T. A. Kunkel, M. A. Resnick, D. A. Gordenin, The 3′→5′ exonuclease of DNA polymerase δ can substitute for the 5′ flap endonuclease Rad27/Fen1 in processing Okazaki fragments and preventing genome instability. *Proc. Natl. Acad. Sci. U.S.A.* **98**, 5122–5127 (2001).
31. Y. H. Jin, R. Ayyagari, M. A. Resnick, D. A. Gordenin, P. M. J. Burgers, Okazaki fragment maturation in yeast:II. Cooperation between the polymerase and 3′–5′-exonuclease activities of Pol δ in the creation of a ligatable nick. *J. Biol. Chem.* **278**, 1626–1633 (2003).
32. P. Garg, C. M. Stith, N. Sabouri, E. Johansson, P. M. Burgers, Idling by DNA polymerase δ maintains a ligatable nick during lagging-strand DNA replication. *Genes Dev.* **18**, 2764–2773 (2004).
33. J. L. Stodola, P. M. Burgers, Resolving individual steps of Okazaki-fragment maturation at a millisecond timescale. *Nat. Struct. Mol. Biol.* **23**, 402–408 (2016).
34. K. I. Kao, L. A. Henricksen, Y. Liu, R. A. Bambara, Cleavage specificity of *Saccharomyces cerevisiae* flap endonuclease 1 suggests a double-flap structure as the cellular substrate. *J. Biol. Chem.* **277**, 14379–14389 (2002).
35. E. Friedrich-Heineken, G. Henneke, E. Ferrari, U. Hübscher, The acetylatable lysines of human Fen1 are important for endo- and exonuclease activities. *J. Mol. Biol.* **328**, 73–84 (2003).
36. S. P. Bell, K. Labib, Chromosome duplication in *Saccharomyces cerevisiae*. *Genetics* **203**, 1027–1067 (2016).
37. F. W. Zheng, R. E. Georgescu, H. L. Li, M. E. O'Donnell, Structure of eukaryotic DNA polymerase δ bound to the PCNA clamp while encircling DNA. *Proc. Natl. Acad. Sci. U.S.A.* **117**, 30344–30353 (2020).
38. K. Shimada, M. Tsai-Pflugfelder, N. D. Vijeh Motlagh, N. Delgoshaie, J. Fuchs, H. Gut, S. M. Gasser, The stabilized Pol31-Pol3 interface counteracts Pol32 ablation with differential effects on repair. *Life Sci. Alliance* **4**, e202101138 (2021).
39. C. H. Yu, H. Gan, A. Serra-Cardona, L. Zhang, S. Gan, S. Sharma, E. Johansson, A. Chabes, R.-M. Xu, Z. Zhang, A mechanism for preventing asymmetric histone segregation onto replicating DNA strands. *Science* **361**, 1386–1389 (2018).
40. B. J. Thomas, R. Rothstein, Elevated recombination rates in transcriptionally active DNA. *Cell* **56**, 619–630 (1989).
41. C. J. Viggiani, O. M. Aparicio, New vectors for simplified construction of BrdU-Incorporating strains of *Saccharomyces cerevisiae*. *Yeast* **23**, 1045–1051 (2006).
42. R. Zellweger, M. Lopes, Dynamic architecture of eukaryotic DNA replication forks in vivo, visualized by electron microscopy. *Methods Mol. Biol.* **1672**, 261–294 (2018).
43. J. M. Sogo, F. Thoma, Electron microscopy of chromatin. *Methods Enzymol.* **170**, 142–165 (1989).
44. Z. Xu, J. Feng, Q. Li, Measuring genome-wide nascent nucleosome assembly using RelN-map. *Methods Mol. Biol.* **2196**, 117–141 (2021).
45. S. F. Liu, Z. Xu, H. Leng, P. Zheng, J. Yang, K. Chen, J. Feng, Q. Li, RPA binds histone H3-H4 and functions in DNA replication-coupled nucleosome assembly. *Science* **355**, 415–420 (2017).
46. Y. J. Shyu, C. D. Hu, Fluorescence complementation: An emerging tool for biological research. *Trends Biotechnol.* **26**, 622–630 (2008).
47. M. E. Levenstein, J. T. Kadonaga, Biochemical analysis of chromatin containing recombinant *Drosophila* core histones. *J. Biol. Chem.* **277**, 8749–8754 (2002).
48. X. Z. Wang, Y. Tang, J. Xu, H. Leng, G. Shi, Z. Hu, J. Wu, Y. Xiu, J. Feng, Q. Li, The N-terminus of Spt16 anchors FACT to MCM2-7 for parental histone recycling. *Nucleic Acids Res.* **51**, 11549–11567 (2023).
49. T. T. Chen, X. Chen, S. Zhang, J. Zhu, B. Tang, A. Wang, L. Dong, Z. Zhang, C. Yu, Y. Sun, L. Chi, H. Chen, S. Zhai, Y. Sun, L. Lan, X. Zhang, J. Xiao, Y. Bao, Y. Wang, Z. Zhang, W. Zhao, The genome sequence archive family: Toward explosive data growth and diverse data types. *Genom. Proteom. Bioinf.* **19**, 578–583 (2021).
50. CNCB-NGDC Members and Partners, Database resources of the national genomics data center, China national center for bioinformation in 2022. *Nucleic Acids Res.* **50**, D27–D38 (2022).

Acknowledgments: We thank D. Kong at Peking University (PKU) for instructing with electron microscopy sample preparations. We thank X. Hao and Y. Liu at the electron microscope platform of PKU and the National Center for Protein Sciences (PKU) for assisting with electron microscopy data collection. **Funding:** This work was supported by the National Key Research and Development Program (2019YFA0508900 to Q.L.), National Natural Science Foundation of China (NSFC 32370623 to J.F. and NSFC 31830048 and 31725015 to Q.L.) and the Beijing Outstanding Young Scientist Program (BJJWZYJH01201910001005 to Q.L). **Author contributions:** Writing—original draft: G.S., C.Y., J.W., J.F., and Q.L. Conceptualization: G.S., C.Y., J.W., J.F., and Q.L. Investigation: G.S., C.Y., J.W., J.H., J.F., and Q.L. Writing—review and editing: G.S., C.Y., J.W., J.F., and Q.L. Methodology: G.S., C.Y., Y.L., J.H., J.F., and Q.L. Resources: G.S., C.Y., and Q.L. Funding acquisition: J.F. and Q.L. Supervision: J.F. and Q.L. **Competing interests:** The authors declare that they have no competing interest. **Data and materials availability:** All data needed to evaluate the conclusions in the paper are present in the paper and/or the Supplementary Materials. The raw sequence data reported here have been deposited in the Genome Sequence Archive (*49*) in the National Genomics Data Center (*50*), China National Center for Bioinformation/Beijing Institute of Genomics, Chinese Academy of Sciences (GSA: CRA014540), and are accessible at https://ngdc.cncb.ac.cn/gsa/.

Submitted 23 January 2024
Accepted 5 July 2024
Published 9 August 2024
10.1126/sciadv.ado1739